Supporting Information

Electronically Coupled Metastable Rh-Engineered NiCo-LDH Fibers for Efficient Alkaline and Seawater Electrolysis

Sreenivasan Nagappan,[a] Partha Pratim Borah,[b] Suprobhat Singha Roy,[a] Prasita Mazumder,[a] Kalishankar Bhattacharyya,[b]* and Subrata Kundu[a]*

[a]Academy of Scientific and Innovative Research (AcSIR), Ghaziabad-201002, India.Electrochemical Process Engineering (EPE) Division, CSIR-Central Electrochemical Research Institute (CECRI), Karaikudi-630003, Tamil Nadu, India.

[b]Department of Chemistry, Indian Institute of Technology Guwahati, Guwahati 781039, Assam, India

*E-mail: ksb@iitg.ac.in, skundu@cecri.res.in; kundu.subrata@gmail.com

This file contains 67 pages in which the details of reagents, methods of synthesis, electrochemical characterizations, electrochemical results, and characterizations like EDS spectrum of FESEM, HR-TEM images,

No. of Figures: 39

No. Tables: 9

Reagents and Instrumentation

Sigma-Aldrich was used for the purchase of Nickel chloride ($NiCl_2.6H_2O$), Cobalt chloride ($CoCl_2.6H_2O$), Urea, Rhodium (III) chloride**,** and Ammonium fluoride (NH_4F). A lab coat, gloves, mask, safety goggles, and shoes are strongly advised for handling the chemicals to ensure safety hazard control. All electrochemical characterizations were performed using the electrochemical analyzer AUT-M204. We bought a Hg/HgO reference electrode from CH Instruments with an internal solution of 1 M KOH. As counter and working electrodes, carbon cloth (CC) and Carbon fiber (CF) were utilized from Alfa Aesar, respectively. The synthesized material was subjected to various characterization studies such as FE-SEM (make: Carl Zeiss; model: SUPRA 55VP), HR-TEM (make: FEI, Netherlands; model: TalosF200S with Gatan EELS), powder X-ray diffractometer (PXRD) (make: Rigaku; model: smart lab XRD) and X-ray photoelectron spectroscopy (XPS) [make: Thermo Fisher Scientific; model: ESCA lab 250], X-ray adsorption near edge structure (XANES). Inductively coupled plasma–optical emission spectrometry (ICP-OES) [PerkinElmer Optima 5300 DV], was carried out to analyze the number of metal ions present in the catalysts.

Electrochemical Characterizations for three-electrode system:

Electrochemical measurements: The electrochemical properties were measured using a Metrohm AUTOLAB-M240 instrument with techniques like CV, LSV, and EIS. All the electrochemical experiments were carried out by employing a conventional three-electrode set-up. (Hg/HgO reference (1 M KOH internal solution), carbon cloth-counter, and carbon fiber (CF) as working electrode). The working electrodes were fabricated using 1 mg of polyvinylidene fluoride (PVDF) as a binder and N-Methyl-2-pyrrolidone (NMP) as a slurry preparation agent. Typically, the ≈4:1 (with respect to overall catalyst loading over the electrode surface) ratio of catalyst and

PVDF was taken into a mortar, followed by the addition of NMP solvent with continuous mixing by a pestle. Then, a certain amount of catalyst ink was fabricated over the 1 cm^2 area of the carbon fiber (CF). The amount of loaded catalyst was calculated by measuring the difference in weight of coated and uncoated carbon fiber (CF). The polarization studies were carried out at a slow scan rate of 5 mV/sec. 100 % iR compensation was done manually from the R_u from EIS. The electrochemical impedance studies were carried out in the frequency range of 0.1 Hz to 100 kHz.

Calibration of the Reference electrode

The significance of the reference calibration electrode is to make the measured data more accurate and repeatable, and to minimize human errors. In this work, H_2 purging was used to calibrate the reference electrode. The principle of H_2 correction is that the hydrogen evolution reaction (HER) reaction occurs when the voltage is less than 0V vs RHE, the hydrogen oxidation reaction (HOR) reaction occurs when the voltage is greater than 0 V, and the current is 0 A when the voltage is 0 V. Use Hg/HgO (SHE 0.098V) electrode and 1 M KOH electrolyte to describe the calibration process in detail.

The steps are as follows:

a) Find a useful Hg/HgO reference electrode.
b) Estimate the potential interval. According to the estimation of E(RHE) = E(SHE) + 0.059 pH, in 1 M KOH, what is the approximate value of E(RHE) (0.924 V for Hg/HgO);
c) Equipped with electrolyte. (1 M KOH)
d) Purging with pure H_2 for 30 minutes. (Be sure to pay attention to safety! Use a fume hood and a gas sensor. The time is related to the flow rate. If it is too small, consider air backflow.

If the electrolyte is too large, it will evaporate. It is recommended to seal with plastic wrap.)

e) Connect the circuit. Both the working electrode and the counter electrode are made of platinum, and the reference electrode is Hg/HgO;

f) 0 A point test. The electrochemical workstation makes a CV curve around the estimated E(RHE) value, Pre-scan to find the approximate position of 0 A, - 0.875~-0.975V, the scanning speed can be 5 $mV \cdot s^{-1}$, and it is found that the potential of 0 A is about -0.924 V; Reduce the CV range: -0.915~-0.935V, sweep speed 1$mV \cdot s^{-1}$, take the average of the positive and negative sweep intersection points, and the general difference is 1mV. Pay attention to the test at least 3 times. If the coincidence is not good, it means that the H_2 purge is insufficient. Increase the flow and continue to step d.

$$E_{HOR(vs\ RHE)} = E_{Hg/HgO}^{o} + E_{Hg/HgO}^{calibrated} + \frac{2.303RT}{F} \times pH \quad \text{……equation S1}$$

where $\frac{2.303RT}{F}$ was calculated for each temperature point.

Overpotential

For OER in 1 M KOH solution, the commercial Hg/HgO (1 M KOH internal solution) and graphite were used as reference and counter electrodes, respectively.

$E_{RHE} = E_{ref} + 0.099\ V + 0.059pH$ (at 25°C) (S1)

$E_{RHE} = E_{ref} + 0.088\ V + 0.0600pH$ (at 30°C) (S2)

$E_{RHE} = E_{ref} + 0.075\ V + 0.0622pH$ (at 40°C) (S3)

$E_{RHE} = E_{ref} + 0.063\ V + 0.0639pH$ (at 50°C) (S4)

$E_{RHE} = E_{ref} + 0.049\ V + 0.0655\ pH$ (at 60°C) (S5)

$E_{RHE} = E_{ref} + 0.035\ V + 0.0669pH$ (at 70°C) (S6)

All the potential data were converted into an RHE scale:

$E_{RHE} = E_{appl} + E_{ref} + 0.059pH$ (S7)

Whereas E_{RHE} is the converted cell potential, E_{appl} is the applied potential, E_{ref} is the cell potential of the reference electrode employed. Later, all the potential data were converted concerning a reversible hydrogen electrode (RHE). Overpotential is calculated by using the formula

$\eta = E_{RHE} - 1.23\ V$ (S8)

The overpotential values of all the catalysts were calculated at a benchmarking current density of 10 mA cm^{-2} by employing the following relation. The standard electrode potential of the water oxidation reaction decreases with temperature. So, when determining overpotentials (η) during OER at high temperatures (e.g., 25–70 °C), be sure to subtract the corrected E°(T) and not just the 1.23 V.

$\eta = E_{app} - E^0(T)$ (S9)

The Tafel Slope

Tafel slope talks about the relation between the applied overpotential and current density on a log scale, and the corresponding plots are called the Tafel plot. Tafel slope values are derived from the Butler-Volmer equation, which can be represented as

$h = b \times \log(j) + a$ (S10)

$b = (h - a)/[\log(j)]$ (S11)

whereas b, h, j, and a are represented as a Tafel slope, overpotential, current density and reaction constant, respectively. Hence, equation (V) suggests that the current density is inversely proportional to the Tafel slope.

Electrochemical Active Surface Area (ECSA)

The electrochemically active surface areas (ECSA) were measured by determining the

electrochemical C_{dl} using the following equations:

$$i_c = \nu \times C_{dl} \quad \text{(S12)}$$

$$\text{ECSA} = C_{dl}/C_s \quad \text{(S13)}$$

where "i_c" indicates the double-layer charging current resulting from scan-rates (ν) dependent CVs at non-faradic potential, and "Cs" denotes a specific capacitance value of 0.040 mF $cm^{-2,}$ depending on the typical reported values.

Mass Activity

Mass activity for the oxygen evolution reaction (OER) is calculated as the current generated per unit mass of the catalyst at a given overpotential (1.55 V vs. RHE for OER). The general formula is:

$$\text{Mass Activity } \left(Ag^{-1}\right) = \frac{j}{m} \quad \text{(S14)}$$

Where:

- j is the current density measured during the OER experiment.
- m is the mass of the catalyst (g) loaded onto the electrode.

Turnover frequency (TOF)

Calculation of overpotential is quite important to determine the activity of the catalyst; apart from that, calculation of turnover frequency (TOF) is also necessary to find out the potentiality of a catalyst at a particular overpotential. TOF is simply defined as the number of moles of H_2/O_2 formed per unit time from a catalytically active site. The equation which is used to calculate the TOF value of a catalyst is given below,

$$\text{TOF}=\frac{(J_{ECSA} \times N_A)}{(n \times F \times \tau_{Rh\ atoms\ per\ cm^2})} \quad \text{(S15)}$$

where J is the current density at a certain overpotential, N_A is the Avogadro number, n is the number of electron transfers (OER n = 4 and HER n = 2), F is the Faraday constant, and τ is the number of active sites (Rh site) per cm² (ECSA).[1]

Stability

Stability is a vital criterion when utilizing an electrocatalyst for the commercial production of hydrogen. To evaluate an electrode's stability, two common approaches are potentiostatic or galvanostatic tests, as well as cyclic voltammetry (CV) accelerated degradation studies. In a potentiostatic setup, the current remains fixed while the potential varies over time; conversely, in a galvanostatic setup, the current is held constant while the potential changes. A minimal change in performance of the working electrode during OER or HER indicates good stability for prolonged use. To further evaluate catalyst stability, a continuous stability study can be performed over a period ranging from 12 to 100 hours. This approach allows for a comprehensive assessment of the electrocatalyst's durability under operational conditions, ensuring that it can maintain performance over extended periods, which is crucial for practical applications in hydrogen production

Faradaic Efficiency (FE) for OER

The FE estimated an electrode's effectiveness in producing gas by comparing the experimental amount of O_2 generated to the theoretically expected amount. The FE can be determined using:

$$FE = \frac{Experimental\ mol\ of \frac{H_2}{O_2} gas}{Theoretical\ mol\ of \frac{H_2}{O_2} gas} 100\% \quad \text{(S16)}$$

Faraday's law can calculate the theoretical value of O_2:

$$n = \frac{It}{ZF} \quad \text{(S17)}$$

where *n* denotes the amount of theoretical product produced in mol, *I* is the current in amperes, t is the time in seconds, and z is the number of transferred electrons, i.e., O_2 (z = 4), respectively. The Faraday constant (F) is 96,485 C mol^{-1}. The theoretical values of O_2 can be calculated at 100 mA for 10 ~ 60 min

Faradaic Efficiency (FE) for HER

The FE estimated an electrode's effectiveness in producing gas by comparing the experimental amount of H_2 generated to the theoretically expected amount. The FE can be determined using:

$$FE = \frac{Experimental\ mol\ of \frac{H_2}{O_2} gas}{Theoretical\ mol\ of \frac{H_2}{O_2} gas} 100\% \quad \text{(S18)}$$

Faraday's law can calculate the theoretical value of H_2:

$$n = \frac{It}{ZF} \quad \text{(S19)}$$

where *n* denotes the amount of theoretical product produced in mol, *I* is the current in amperes, t is the time in seconds, and z is the number of transferred electrons, i.e., H_2 ($z = 2$), respectively. The Faraday constant (*F*) is 96,485 C mol^{-1}.

Calculation for TOF for HER

The turnover frequency (TOF) is a key metric to evaluate the catalytic efficiency, representing the number of reactant molecules transformed into products per active site per unit time. For the hydrogen evolution reaction (HER), the TOF can be calculated using the current density and the number of active sites. Here's how to calculate the TOF from the charge (or current) and the number of active sites:

$$TOF = \frac{I}{2F \times N_{active\ sietes}} \quad \text{(S20)}$$

Number of Electrons to the Number of Active Sites

$$N_{active\ sites} = n_e \times N_A \quad \text{(S21)}$$

$n_{e\,=}\, n_e$ is the number of moles of electrons

N_A = Avogadro's number (6.022×10^{23} mol^{-1})

2.11 Calculation of d-spacing and lattice constant value: The d-spacing and lattice parameter values of four catalysts were calculated by using the following formulae.

$d = n\lambda\ 2dSin\theta$…….. (S22)

$a = d \times \sqrt{h\ 2 + k\ 2 + l\ 2}$……..

Materials Synthesis

NiCo-LDH powders

In a typical synthesis, a NiCo-LDH catalyst was prepared through hydrothermal routes as described earlier for NiCo-LDHs, NiRu-LDHs, and NiFe-LDHs with a simple modification**.** In a typical synthesis, a 2:1 ratio of $NiCl_2 \cdot 6H_2O$, $CoCl_2.6H_2O$, and 250 mg of NH_4F was dissolved in 40 mL of ultrapure water. Next, 520.2 mg of urea was added to the pea-green solution before mixing completely. Lastly, 15 mL of precursor solution was transferred to a 25 mL Teflon-lined stainless-steel autoclave. The autoclave was heated at 120 ℃ for 12 h in an oven before natural cooling to 25 ℃. The wet powder was extracted by low-speed centrifuging the reactive mixture at 6000 rpm for 10 min. The precipitate was rinsed at least three times with ultrapure water and ethanol and dried at 60 ℃ overnight, and labeled as NiCo-LDH.

Rh/NiCo-LDH powders

The mettalic Rh and Rh_2O_3 NiCo-LDH ($Rh/NiCo-LDH$) catalyst was synthesized via a facile solvothermal reaction. In brief, 1 %, 4% and 7 % Rh were fully dissolved in the centrifuge tube with 14 mL NaOH solution (0.01 M) and 40 mg of NiCo-LDH powder before stirring thoroughly. Then, 1 mL $NaBH_4$ solution (1.0 M) was slowly added dropwise to the suspension and mixed fully. The suspension was transferred to a 25 mL Teflon-lined stainless-steel autoclave, which was heated at 120 ℃ for 2 h in an oven, and then cooled to 25 ℃. Finally, the wet powder was obtained by centrifuging the reaction mixture at 6000 rpm for 10 min. The product was cleaned at least three times with ultrapure water and ethanol, dried at 60 ℃ overnight. The final products were Rh_{nps}/NiCo-LDH (1%), Rh_{SA}-Rh_2O_3-NiCo-LDH (Rh/NiCo-LDH) (4%), and Rh_2O_3-NiCo-LDH (Rh@NiCo-LDH) (7%).[2]

Rh/NiCo-LDH fibers

Typically, the Electrospinning (ES) technique was used for the synthesis of Rh/NiCo-LDH powders incorporated with microfibers. 100 mg of Rh/NiCo-LDH powders was added to 2.3 mL of dimethylformamide (DMF), and the mixture was subjected to ultrasonication to get a dispersed solution. 0.175 g of polyacrylonitrile (PAN) was mixed with the above-mentioned DMF solution and kept stirring for 24 hours. The ES precursor solution was transferred into a 2.5 ml disposable syringe and loaded into the ES instrument. The instrument was operated by fixing some of the parameters, such as a flow rate of 0.6 mL h^{-1}, an applied voltage of 16 kV, and the distance between the aluminum collector and syringe was about 11 cm. To remove the solvent molecules, the collected fiber was dried at 60 ºC for 12 h in a hot air oven and labeled as Rh/NiCo-LDH/F. As like same by adding 100 mg of NiCo-LDH powder, the NiCo-LDH/F has been prepared.

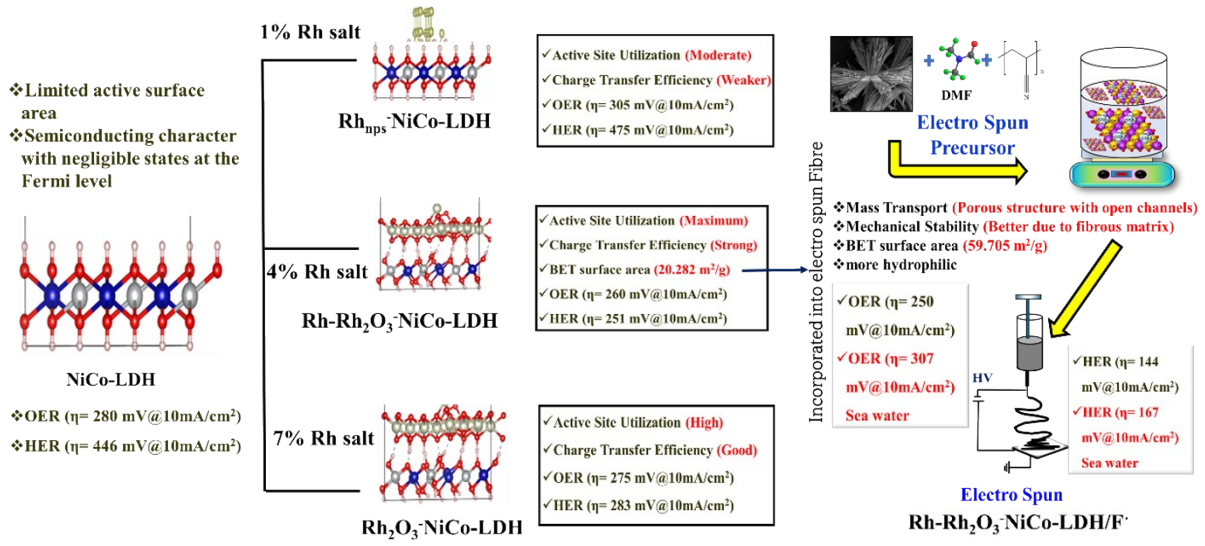

Figure S1. a) Schematic representation of Rh-content-dependent structural evolution in NiCo-LDH and its integration into an electrospun fibrous architecture. Different Rh precursor loadings (1%, 4%, and 7%) yield Rh nanoparticles (Rh_{nps}-NiCo-LDH), Rh–Rh_2O_3 hybrids (Rh/NiCo-LDH), and Rh_2O_3-modified NiCo-LDH (Rh@NiCo-LDH), influencing active site utilization and charge transfer. Incorporation into an electrospun fiber produces a porous, open-channel fiber matrix that enhances mass transport and electrocatalytic performance in both alkaline and sea water electrolysis.

Material Characterization

System	d band Value (eV)		
	Optimized Structure	Bind_O	Bind_OOH
Rh -Rh_2O_3-NiCo surface	-1.590 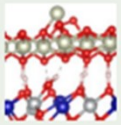	-1.640 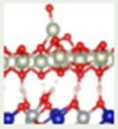	-1.607 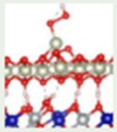
NiCo LDH surface	-2.614 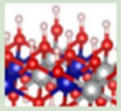	-2.436 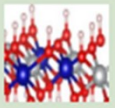	-2.438 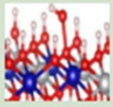

Table S1. Calculated d band vaalue for Rh/NiCo-LDH and NiCo-LDH.

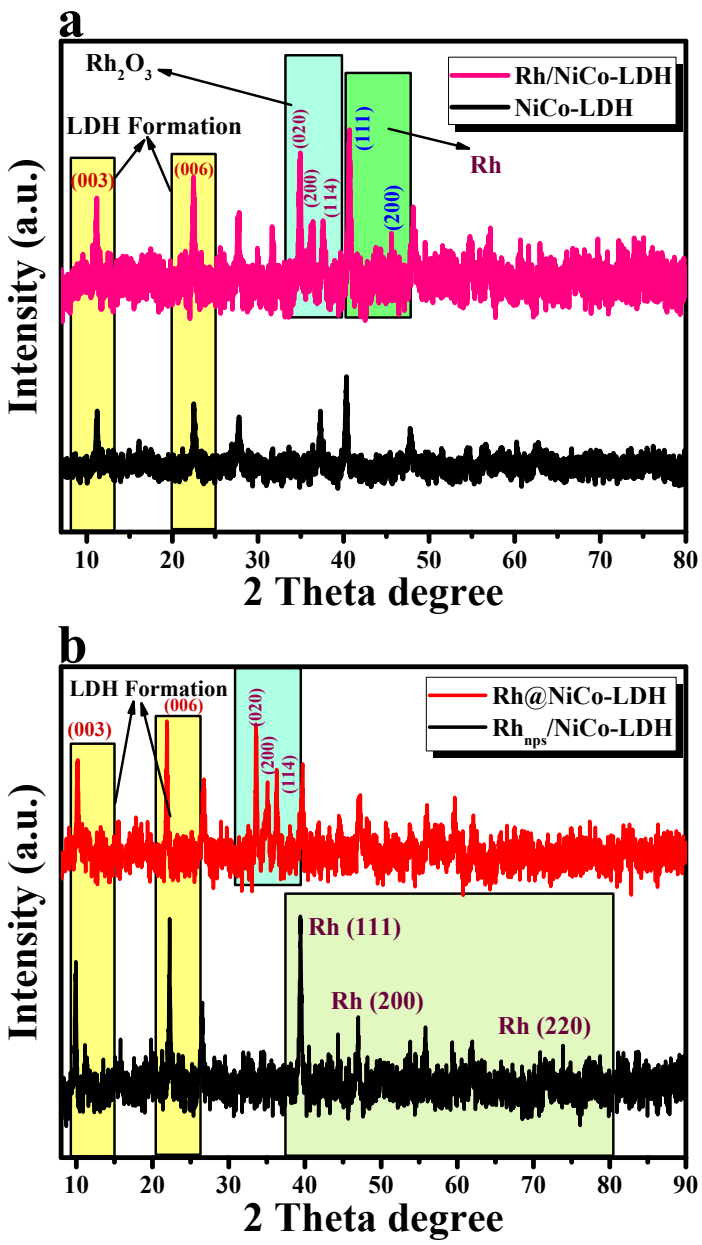

Figure S2. (a) PXRD diffraction pattern of Rh/NiCo-LDH (Rh-Rh_2O_3-NiCo-LDH) and NiCo-LDH, and (b) PXRD diffraction pattern of Rh@NiCo-LDH (Rh@NiCo-LDH) and Rh_{nps}/NiCo-LDH (Rh nanoparticles over NiCo-LDH).

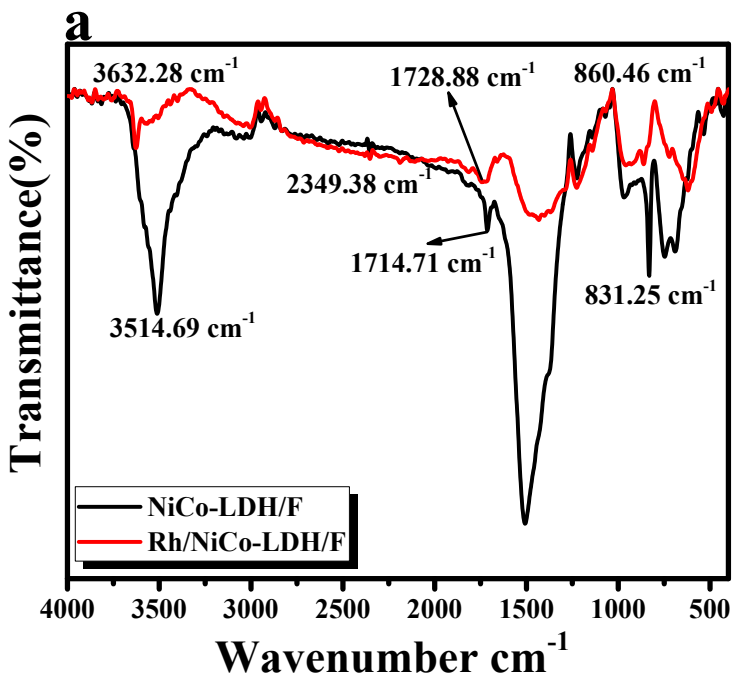

Figure S3. (a) iR-spectrum of Rh/NiCo-LDH/F (Rh-Rh_2O_3-NiCo-LDH incorporated in fiber) and NiCo-LDH/F (NiCo-LDH incorporated in fiber).

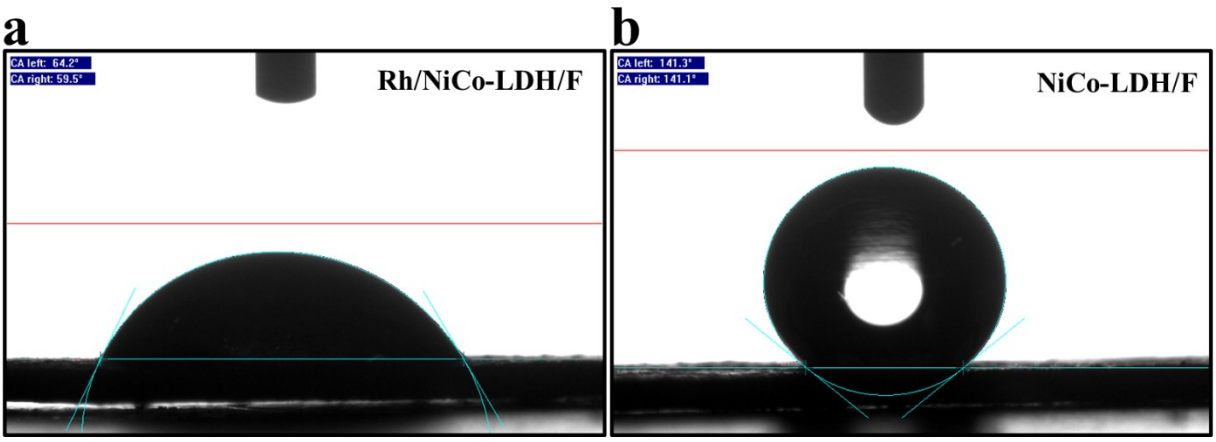

Figure S4. (a-b) contact angle measurements of Rh/NiCo-LDH/F and NiCo-LDH/F.

The hydrophilicity of the synthesized products was examined by contact angle measurements. The lower the value of the contact angle, the better the hydrophilicity, which corresponds to greater water affinity on the catalyst surface. In the present case, the Rh/NiCo-LDH/F exhibited a smaller contact angle than pristine NiCo-LDH/F, indicating that it is more hydrophilic. These results further confirm that the addition of Rh into NiCo-LDH markedly enhances its water adsorption capacity, which is advantageous for electrocatalytic reactions with aqueous electrolytes.

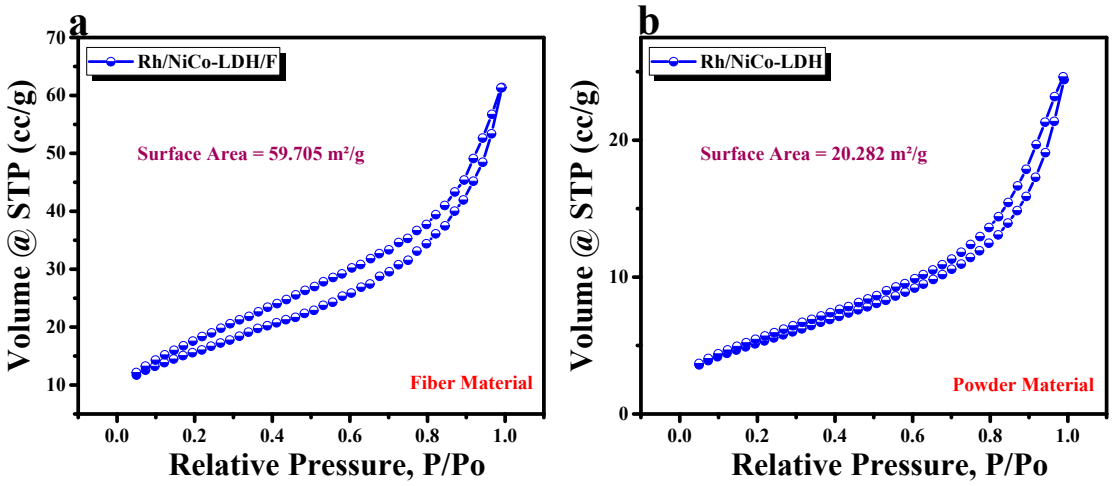

Figure S5. a-b) Brunauer–Emmett–Teller (BET) N_2 adsorption-desorption isotherm analysis for Rh/NiCo-LDH/F (fiber) and Rh/NiCo-LDH (powder).

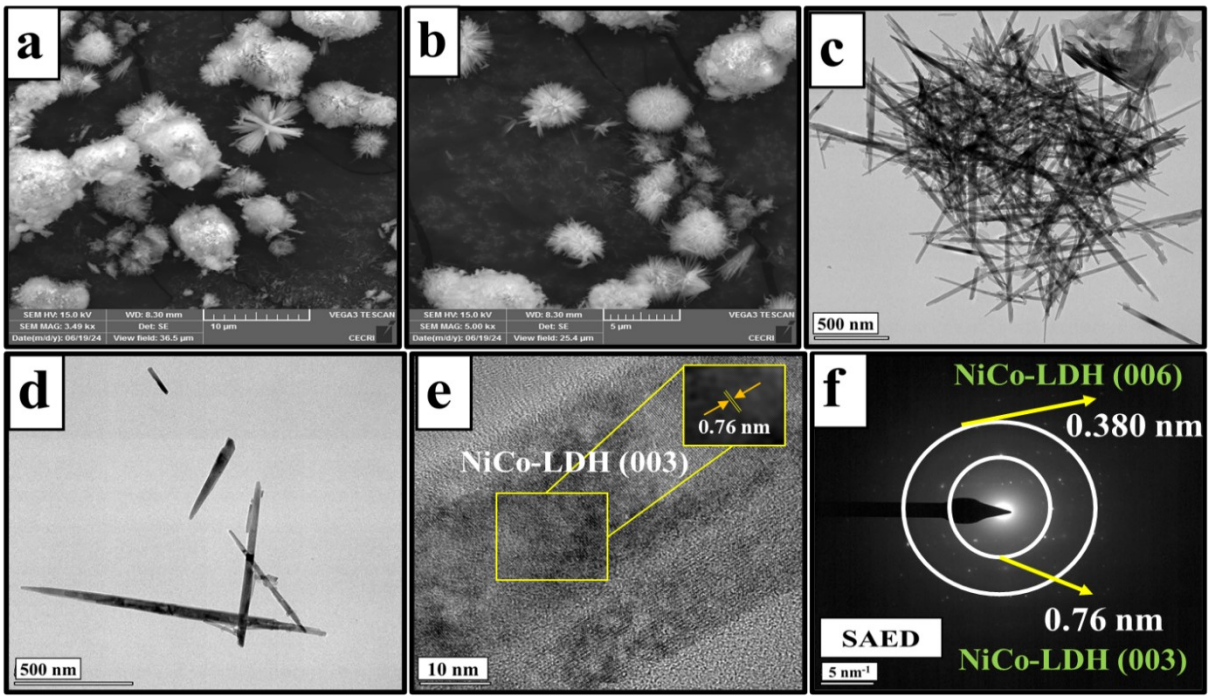

Figure S6. a-b) FE-SEM image of NiCo-LDH (powder), c-d) TEM images of NiCo-LDH (powder), e) HR-TEM lattice fringes pattern of NiCo-LDH (powder), and f) SAED pattern of NiCo-LDH (powder).

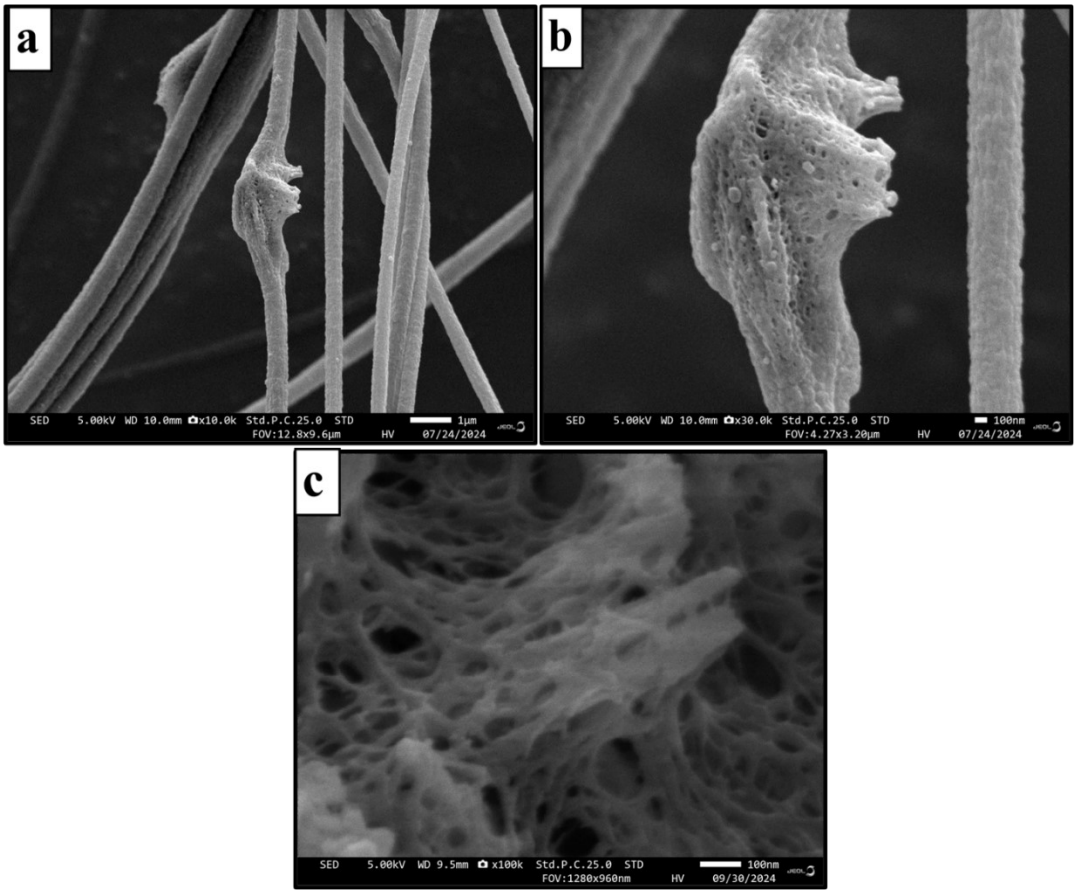

Figure S7. a-c) FE-SEM image of NiCo-LDH (Fiber).

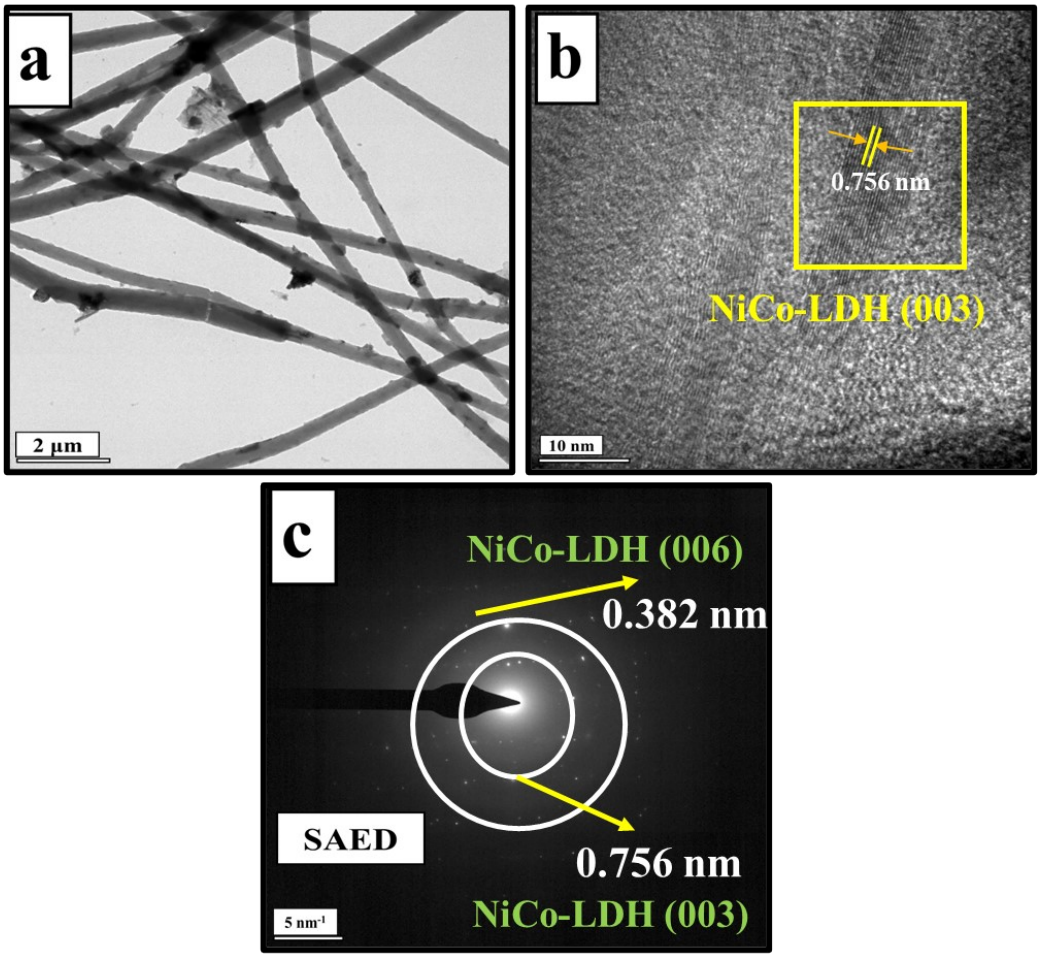

Figure S8. a) TEM images of NiCo-LDH/F, b) HR-TEM lattice fringes pattern of NiCo-LDH/F; and c) SAED pattern of NiCo-LDH/F.

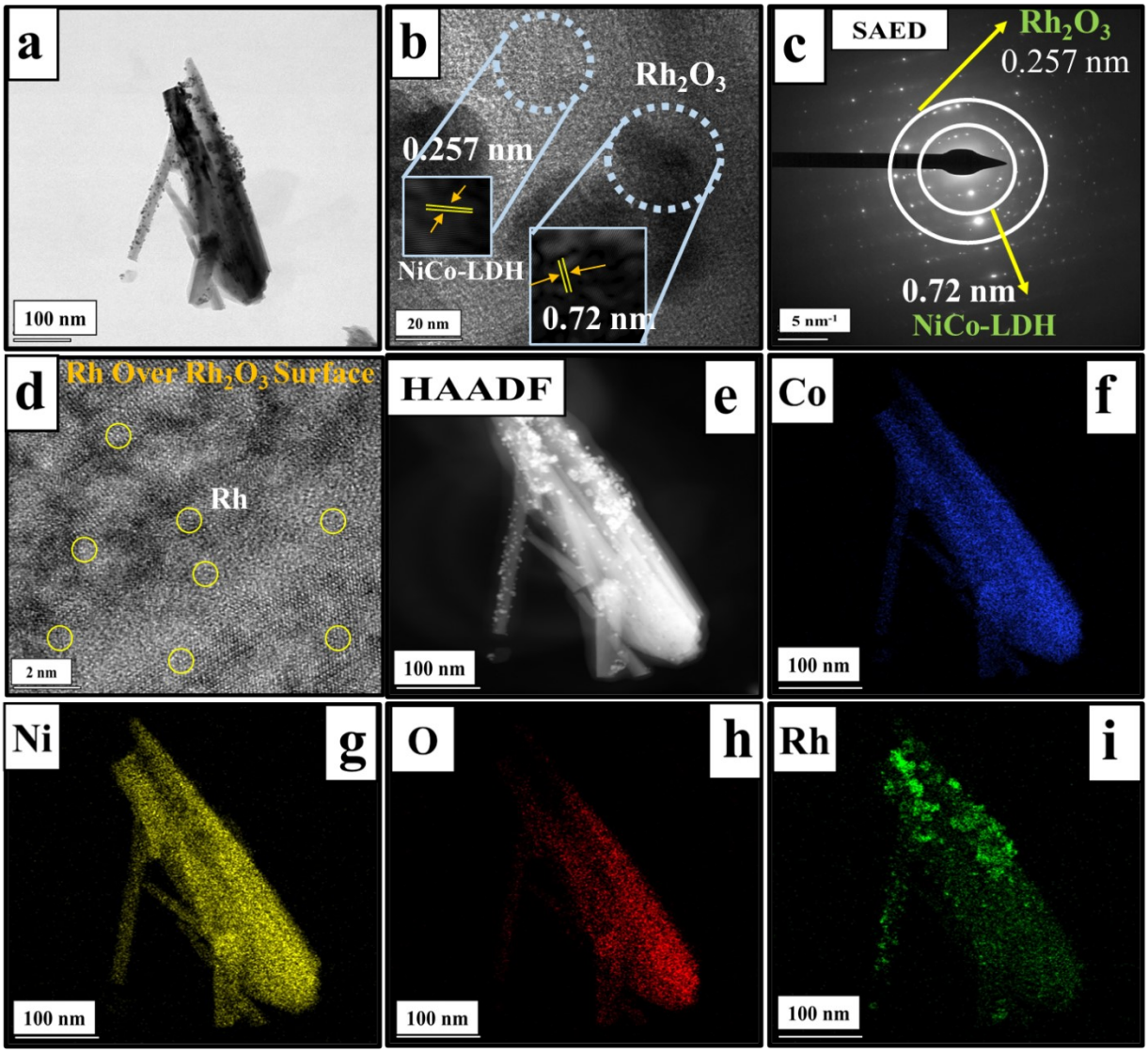

Figure S9. a) TEM images of Rh/NiCo-LDH (powder), b) HR-TEM lattice fringes pattern of Rh/NiCo-LDH (powder), c) SAED pattern of Rh/NiCo-LDH (powder), d) HR-TEM lattice fringes images of Rh/NiCo-LDH (powder), e) HAADF area, and f-i) color mapping results of Rh/NiCo-LDH (powder).

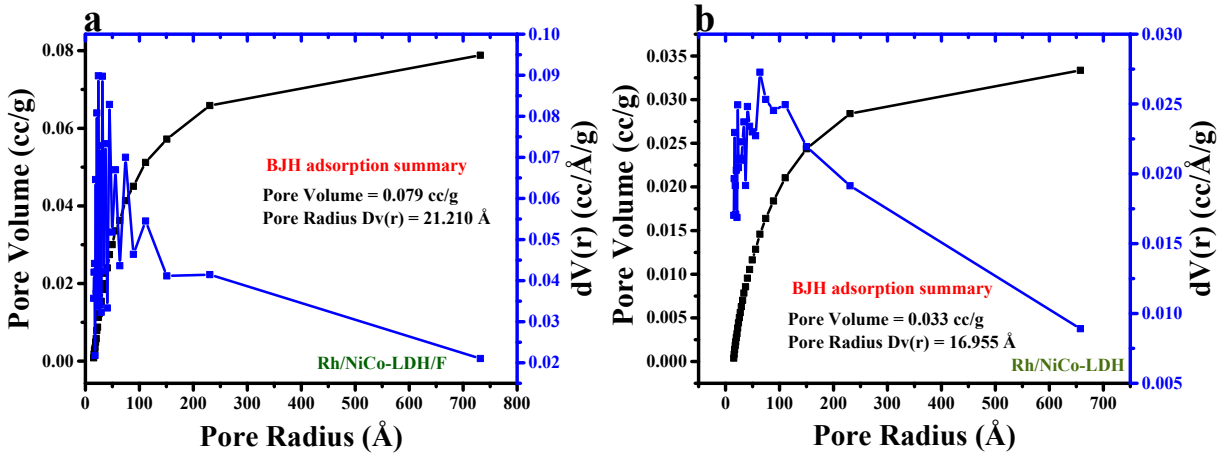

Figure S10. a-b) BJH pore size distribution analysis for Rh/NiCo-LDH/F (Fiber) and Rh/NiCo-LDH (powder).

Catalyst	Ni	Co	Rh
NiCo-LDH	131.881 mg/L	65.297 mg/L	-
Rh/NiCo-LDH	110.786 mg/L	44.856 mg/L	6.482 mg/L
Rh@NiCo-LDH	118.154 mg/L	48.263 mg/L	12.519 mg/L
Rh_{nps}/NiCo-LDH	105.943mg/L	42.852 mg/L	1.502 mg/L

Table S2. ICP-MS analysis of the prepared electrocatalyst.

XPS studies

Figure S11a (supporting information) represents the XPS survey spectrum of NiCo-LDH/F and Rh/NiCo-LDH/F, suggesting the presence of all expected elements. **Figure 3a** depicts the Ni 2p deconvoluted XPS spectra of NiCo-LDH/F and Rh/NiCo-LDH/F. In NiCo-LDH/F peaks at 853.6

and 871.43 eV correspond to Ni^{2+}, while the peaks at 855.4 and 873.2 eV correspond to Ni^{3+} ions. Upon addition of Rh in NiCo-LDH/F, (Rh/NiCo-LDH/F), Ni^{2+} (853.92 and 871.84 eV) and Ni^{3+} (855.8 and 873.7 eV) peaks are shifted towards higher binding energy. This is because Rh, being more electronegative (2.28), withdraws electrons easily from (Ni^{2+}) NiCo-LDH/F. Additionally, an increase in the intensity of the Ni^{3+} peaks in Rh/NiCo-LDH/F further supports the electron transfer from NiCo-LDH/F to the Rh oxides, consistent with electron transfer principles. Figure 3b represents the XPS spectrum of Co 2p, which shows that the peaks of Co3+ (779.18 and 795.01) and Co2+ (781.10 and 796.60) of both materials are present in the same binding energy. This suggests that the Ni site would be the main electron donor to the Rh site in the Rh/NiCo-LDH/F material. Figure 3c shows the XPS spectra of Rh 3d, which indicate the coexistence of metallic Rh and surface oxide species. The peaks at 307.08 eV and 311.80 eV are Rh^0 3d5/2 and 3d3/2, respectively, while peaks at 307.90 eV and 313.05 eV were from Rh^{3+} in Rh–O (III). The negative shift in the binding energy of the Rh^{3+} 3d5/2 peak from the standard value for Rh_2O_3 (308.62 eV) to 307.90 eV represents stronger electronic interactions between the Rh^{3+} species and surrounding oxygen species or the LDH support matrix. **Figure 3d** is the O 1s XPS spectrum of NiCo-LDH, with peaks at 529.33 eV, 530.30 eV, and 531.37 eV, which are assigned to metal oxides, metal hydroxides, and adsorbed H_2O, respectively. The shift to higher binding energy in Rh/NiCo-LDH/F indicates strong electronic interaction between Rh and NiCo-LDH, indicating their efficient heterostructure coupling.[3] The XPS spectrum of N 1s was also discussed for both materials and presented in the Supporting Information (**Figure S11b**).

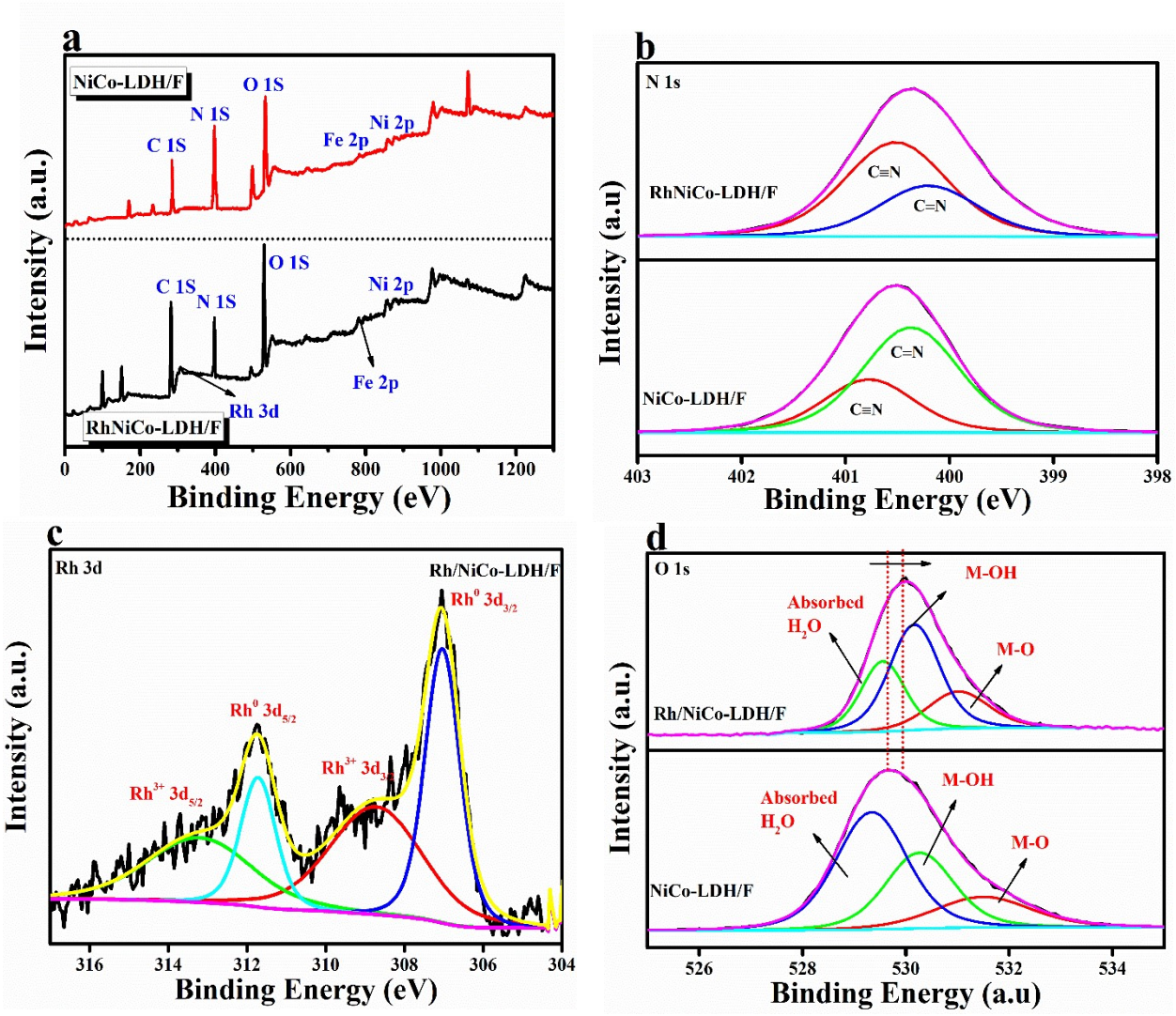

Figure S11. a) XPS survey spectrum for Rh/NiCo-LDH/F and NiCo-LDH/F; b) deconvolated XPS spectrum of N 1S for Rh/NiCo-LDH/F and NiCo-LDH; c) deconvolated XPS spectrum of Rh 3d for Rh/NiCo-LDH/F and NiCo-LDH and d) deconvolated XPS spectrum of O 1S for Rh/NiCo-LDH/F and NiCo-LDH.

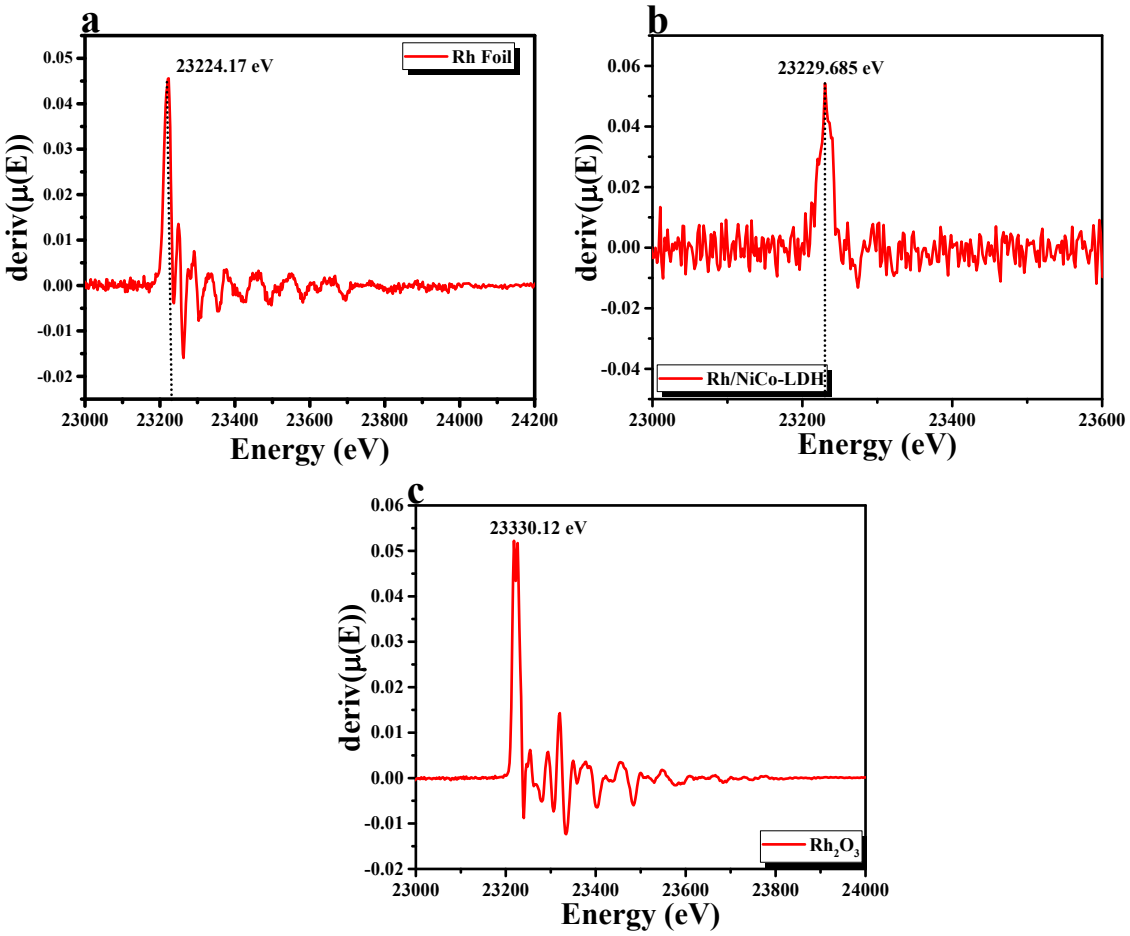

Figure S12. The first derivative curves of the XANES spectra of (a) Rh foil, (b) Ru/NiCo-LDH, and (c) Rh_2O_3

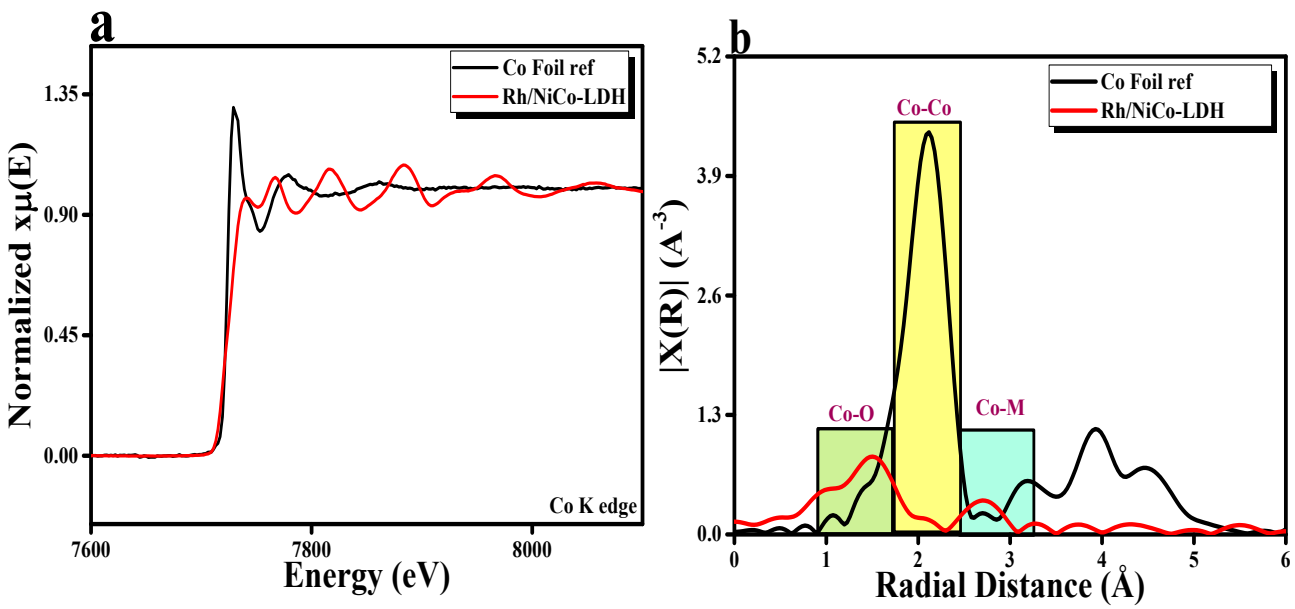

Figure S13. a,) Normalized Co K-edge XANES curves; b) the k3-weighted Fourier transforms of Rh/NiCo-LDH.

Electrocatalytic OER reaction

The electrocatalytic OER activity of Rh/NiCo-LDH and Rh/NiCo-LDH/F was evaluated in an Ar-saturated 1 M KOH solution with a standard three-electrode setup. Cyclic voltammetry (CV) experiments were performed at a scan rate of 5 mV/s, where the backward CV curve was used for analysis.

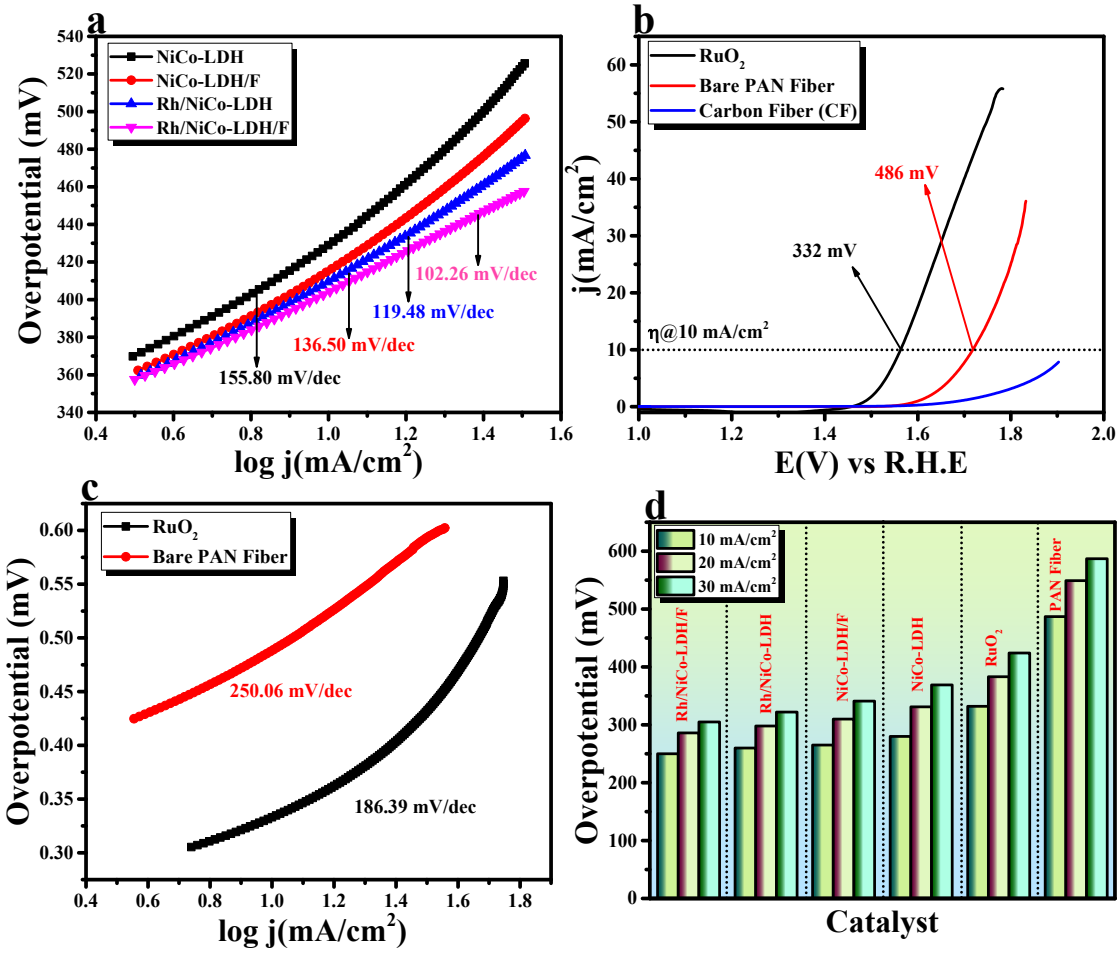

Figure S14. a) Tafel slope of Rh/NiCo-LDH/F, Rh/NiCo-LDH, NiCo-LDH/F and NiCo-LDH; b) LSV polarization curve of RuO_2, bare PAN fiber, and carbon fiber; c) Tafel slope of RuO_2 and bare PAN fiber and overpotential value at different current density.

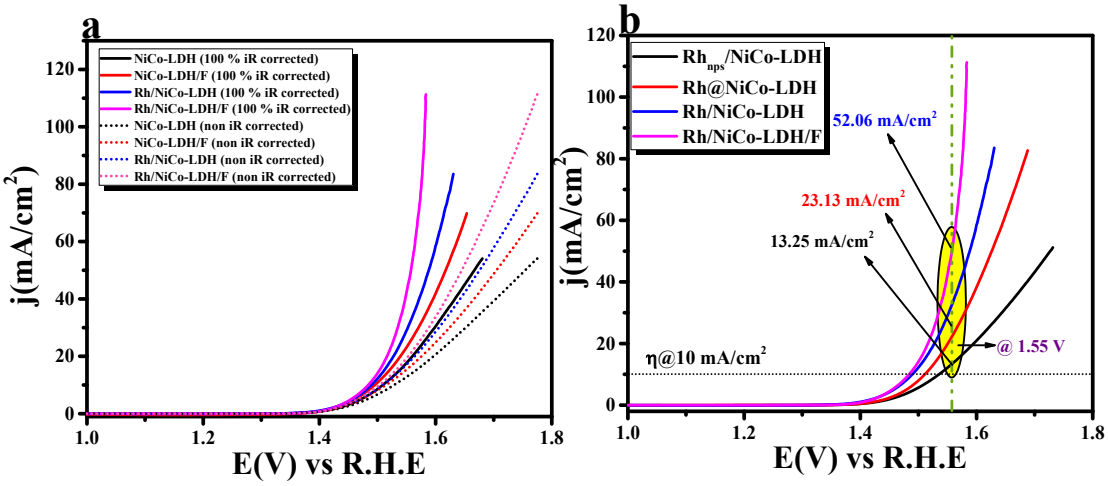

Figure S15. a) LSV polarization curve of Rh/NiCo-LDH/F, Rh/NiCo-LDH, NiCo-LDH/F and NiCo-LDH (iR corrected and non-iR corrected) and b) LSV polarization curve of Rh_{nps}/NiCo-LDH, Rh@NiCo-LDH, Rh/NiCo-LDH and Rh/NiCo-LDH/F.

Catalyst	*Substrate*	*Electrolyte*	*Current density*	**Overpotential**	**Reference**
Rh/NiCo-LDH/F	**Carbon Fiber**	**1 M KOH**	**10 mA/cm^2**	**250 mV**	**This work**
Ru, Ni–CoP porous nanofibers	Glass carbon	1 M KOH	10 mA/cm^2	251 mV	[4]
$Ni_{0.6}Co_{1.4}P$	Glass carbon	1 M KOH	10 mA/cm^2	300 mV	[5]
CeO_2-CoO nanofibers	Glass carbon	1 M KOH	10 mA/cm^2	296 mV	[6]
$CoFe_2O_4$ nanofibers	Glassy carbon	1 M KOH	10 mA/cm^2	340 mV	[7]
OP-$NiFe_2O_4$/NCNF	Glassy carbon electrode	1 M KOH	10 mA/cm^2	260 mV	[8]
NiO/$NiCo_2O_4$ porous nanofibers	Glassy carbon electrode	1 M KOH	10 mA/cm^2	357 mV	[9]
NiFe@LDH	Nickel Foam	1 M KOH	10 mA/cm^2	260 mV	[10]
NiFe-LDH@Ni_3S_2	NF	1 M KOH	10 mA/cm^2	271 mV	[11]

NiMn LDH/$NiCo_2O_4$ nanowires	NF	1 M KOH	10 mA/cm^2	310 mV	[12]
NiFe-LDH/$FeCoS_2$/CFC	Carbon fiber cloth	1 M KOH	10 mA/cm^2	308 mV	[13]
ORDE NiFe LDHs	Cu mesh	1 M KOH	10 mA/cm^2	292 mV	[14]
Ag@NiFe LDHs	CF	1 M KOH	10 mA/cm^2	330 mV	[15]
Co-PBA@NiFe-LDH-30	Glassy carbon	1 M KOH	10 mA/cm^2	253 mV	[16]

Table S3. Comparison table of recently reported OER catalyst in alkaline medium. Note: We have compared our material with both powder and fiber materials

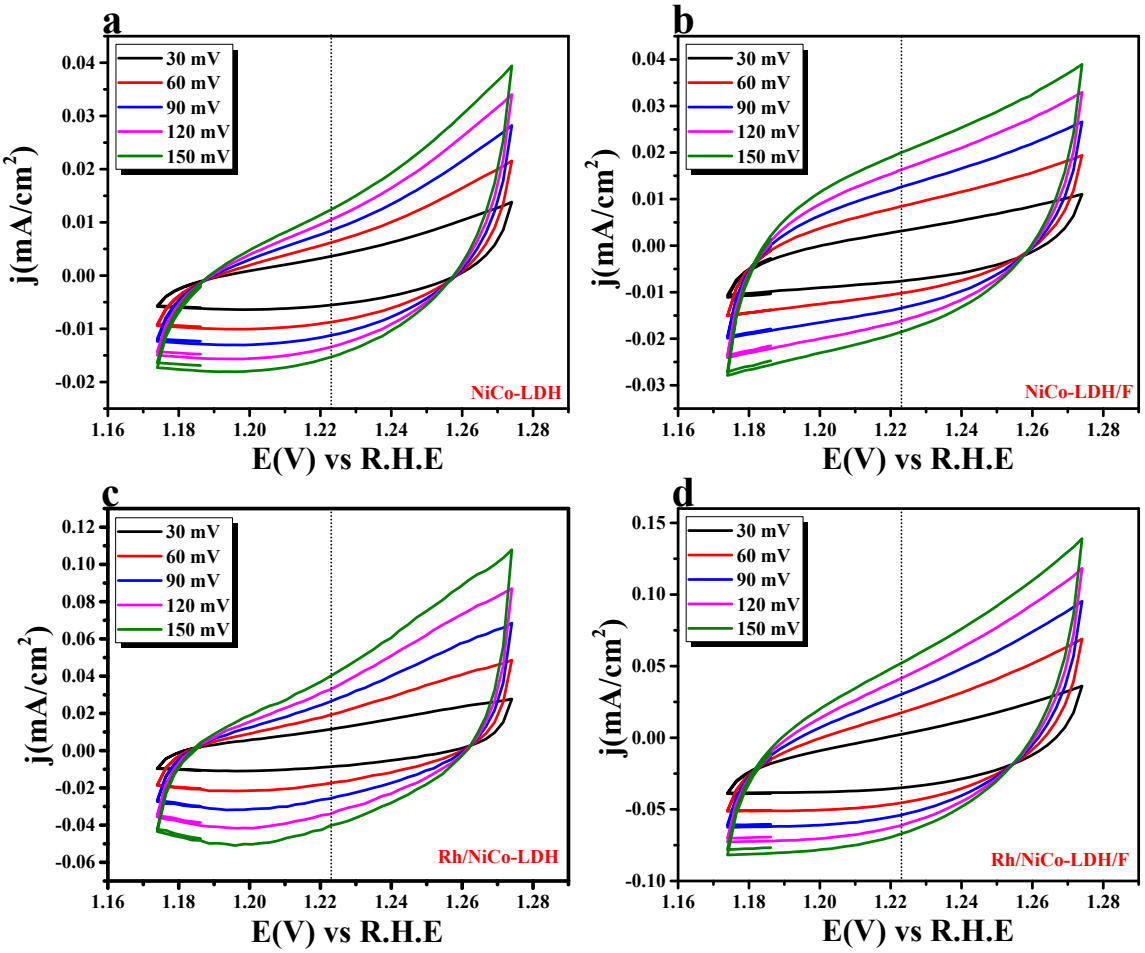

Figure S16. a-d) scan rate-dependent CV curves obtained for calculating the C_{dl} value in the non-faradaic region of 1.18 to 1.27 V vs RHE of NiCo-LDH, NiCo-LDH/F, Rh/NiCo-LDH and Rh/NiCo-LDH/F.

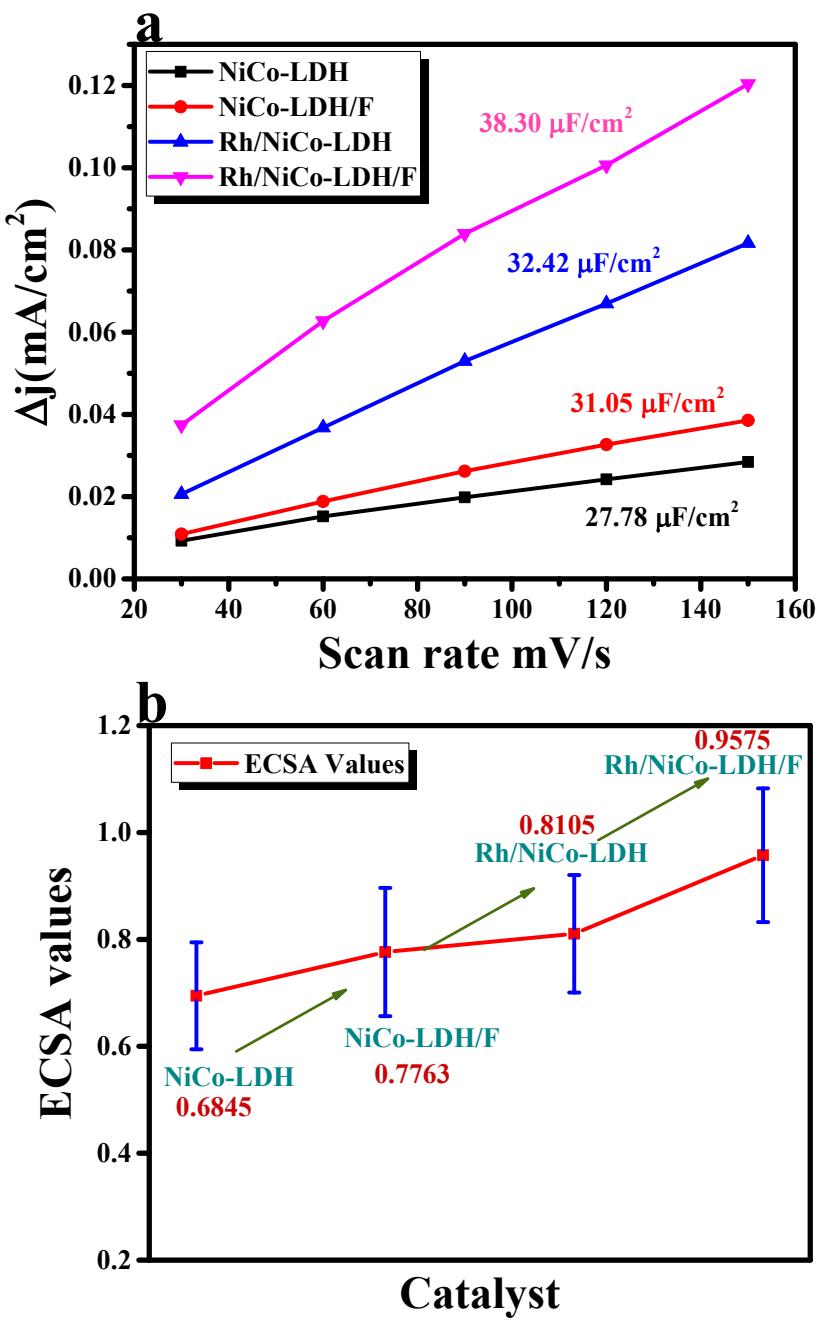

Figure S17. a) ΔJ vs. scan rate plot for obtaining the C_{dl} information, and b) calculated ECSA.

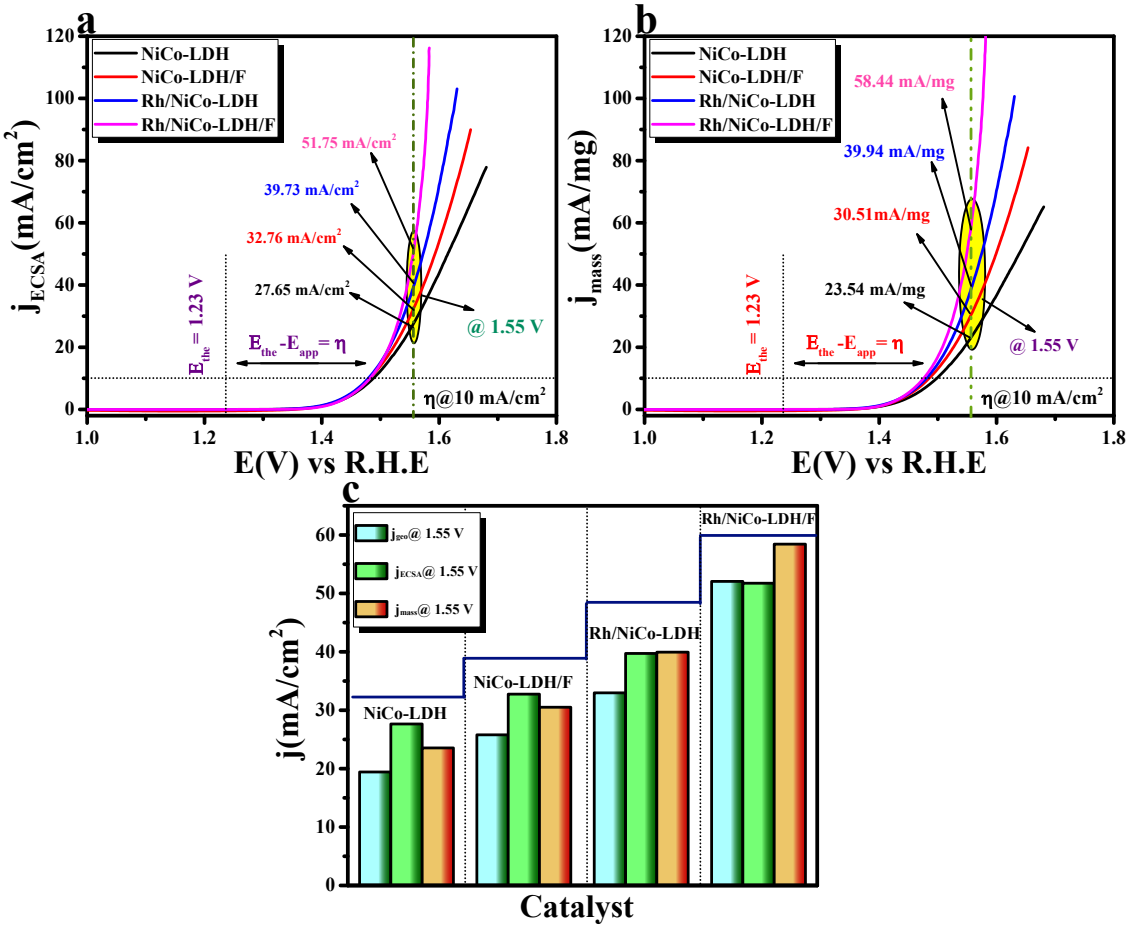

Figure S18. (a) ECSA-normalized LSV polarization curve, (b) mass-normalized LSV polarization curve, and c) current measurement @1.55 V vs R.H.E of NiCo-LDH, NiCo-LDH/F, Rh/NiCo-LDH, and Rh/NiCo-LDH/F.

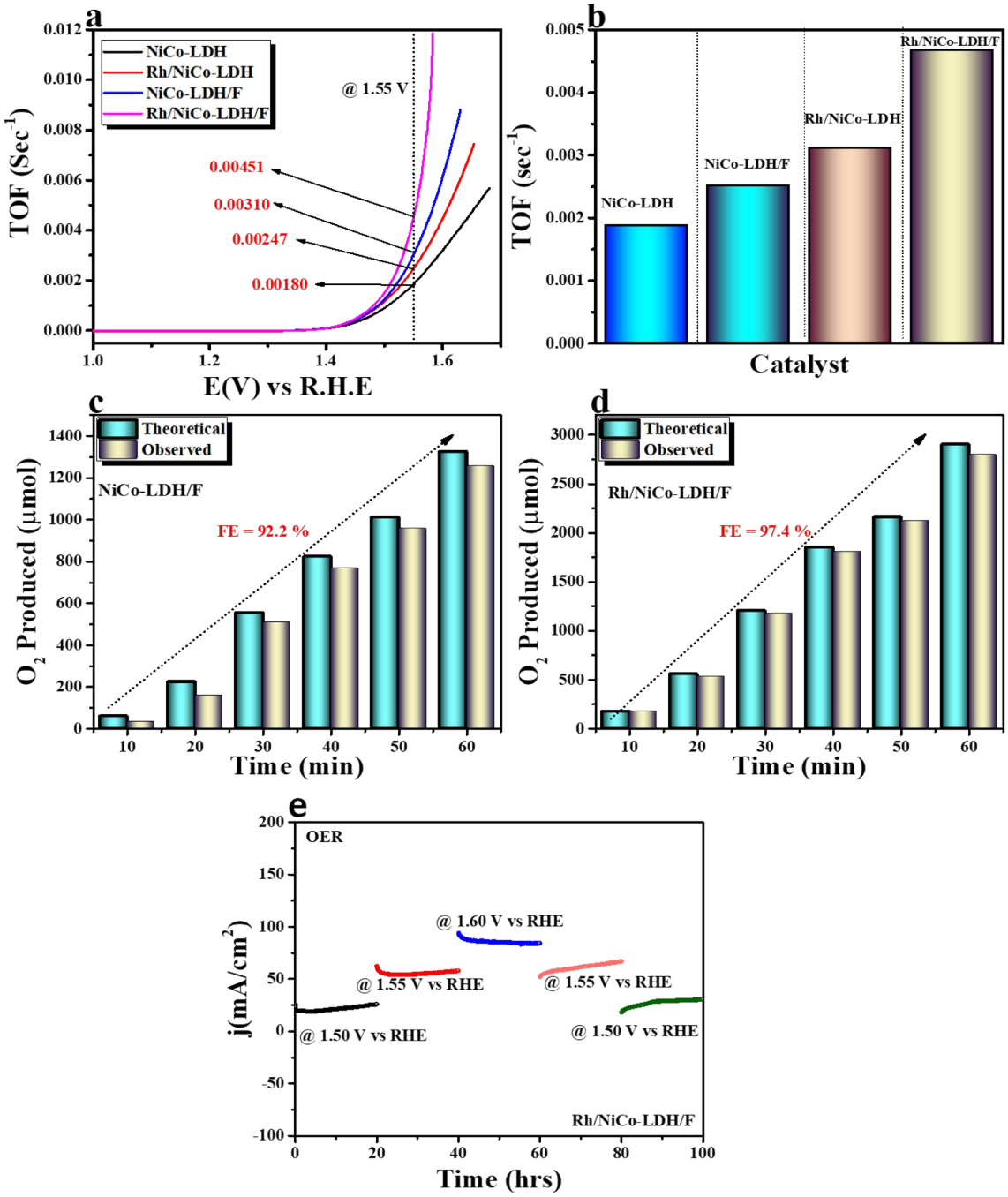

Figure S19. a) calculated TOF value of NiCo-LDH, NiCo-LDH/F, Rh/NiCo-LDH and Rh/NiCo-LDH/F; b) TOF value @1.55V of NiCo-LDH, NiCo-LDH/F, Rh/NiCo-LDH and Rh/NiCo-LDH/F; c-d) Faradaic efficiency and quantitative analysis of produced H_2 in NiCo-LDH/F, Rh/NiCo-LDH/F with different time intervals measured via gas-chromatography and e) chronoamperometry study of Rh/NiCo-LDH/F at different potential.

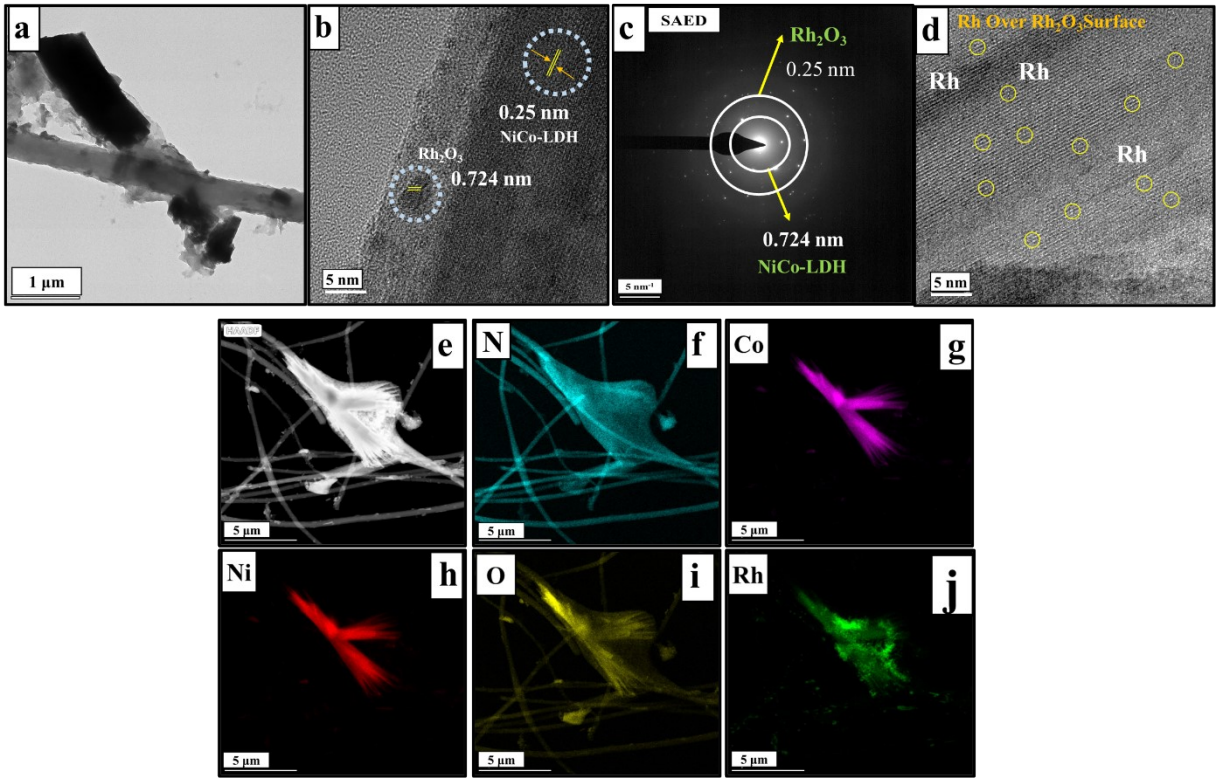

Figure S20. a) TEM images of post-Rh/NiCo-LDH/F; b) HR-TEM lattice fringes pattern of post-Rh/NiCo-LDH/F; c) SAED pattern post-Rh/NiCo-LDH/F; d) HR-TEM images of post-Rh/NiCo-LDH/F; e) HADDAF image of post-Rh/NiCo-LDH/F; and f-j) color mapping results of post-Rh/NiCo-LDH/F.

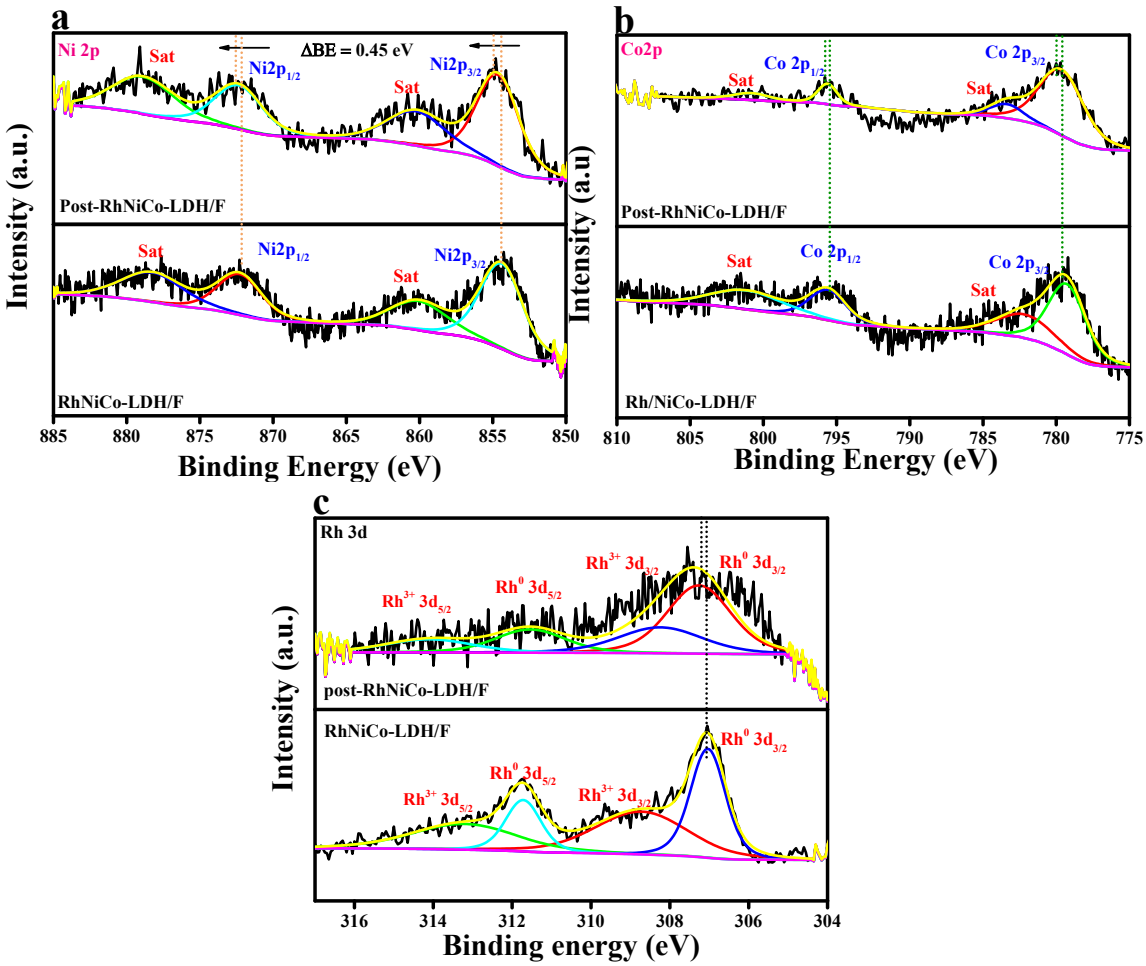

Figure S21. Post -XPS: a) deconvolved XPS spectrum of Ni 2p; deconvolved XPS spectrum of Co 2p and deconvolved XPS spectrum of Rh 3d.

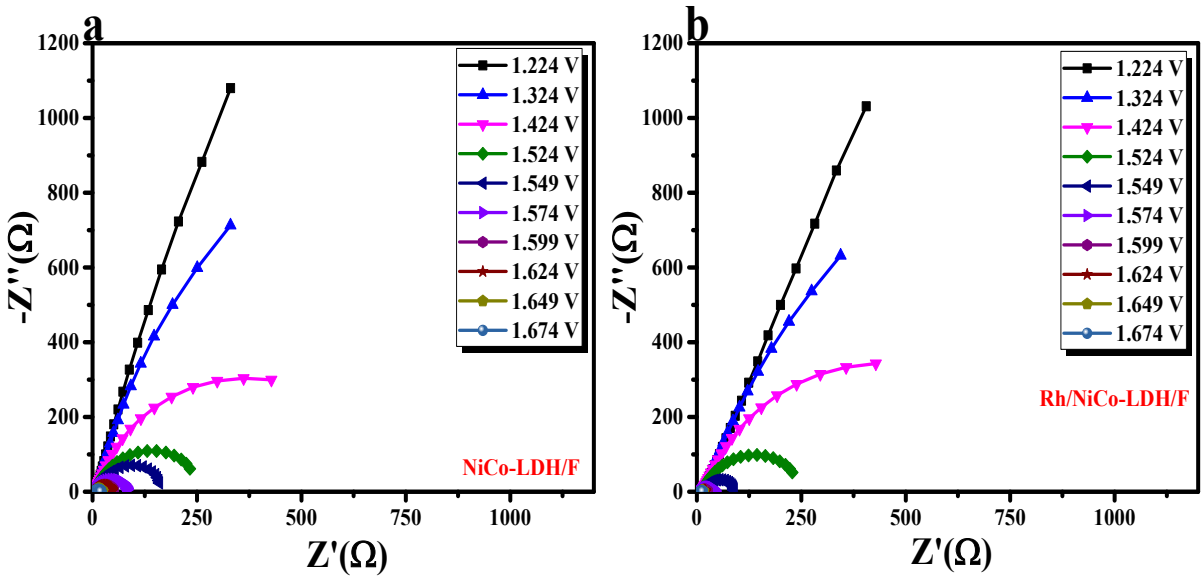

Figure S22. (a,b) Nyquist for NiCo-LDH/F and Rh/NiCo-LDH/F at different applied potentials.

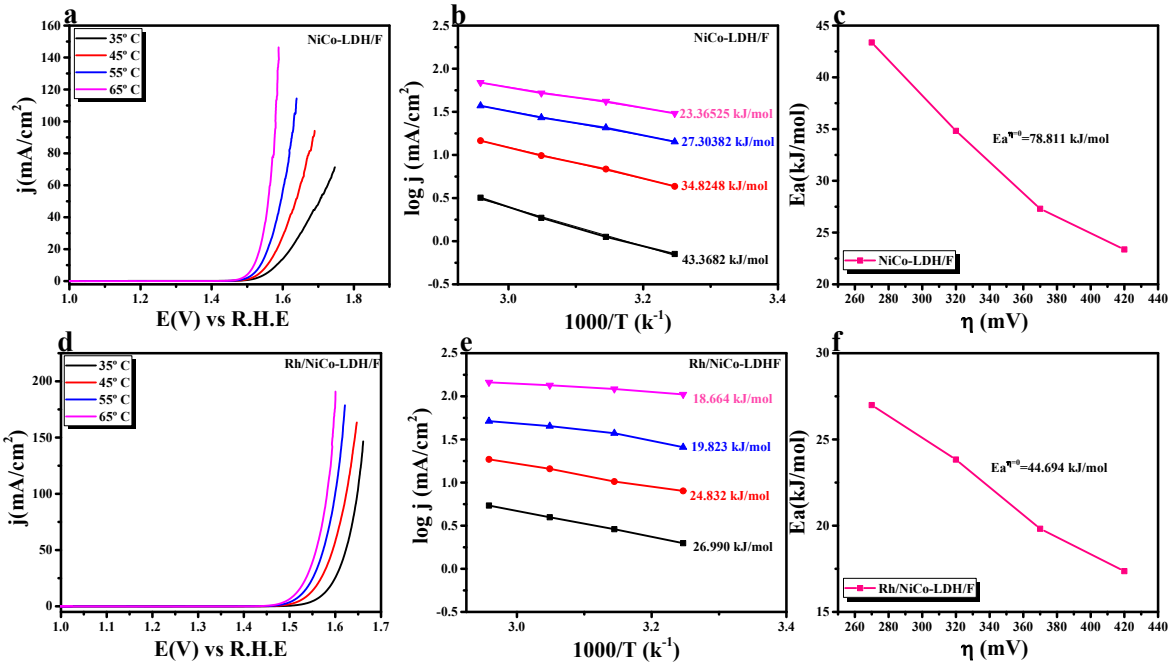

Figure S23. (a, d) temperature dependent LSV polarization curve of NiCo-LDH/F and Rh/NiCo-LDH/F; (b, e) Arrhenius plots for NiCo-LDH/F and Rh/NiCo-LDH/F and c, f) E_a @ zero overpotential for NiCo-LDH/F and Rh/NiCo-LDH/F.

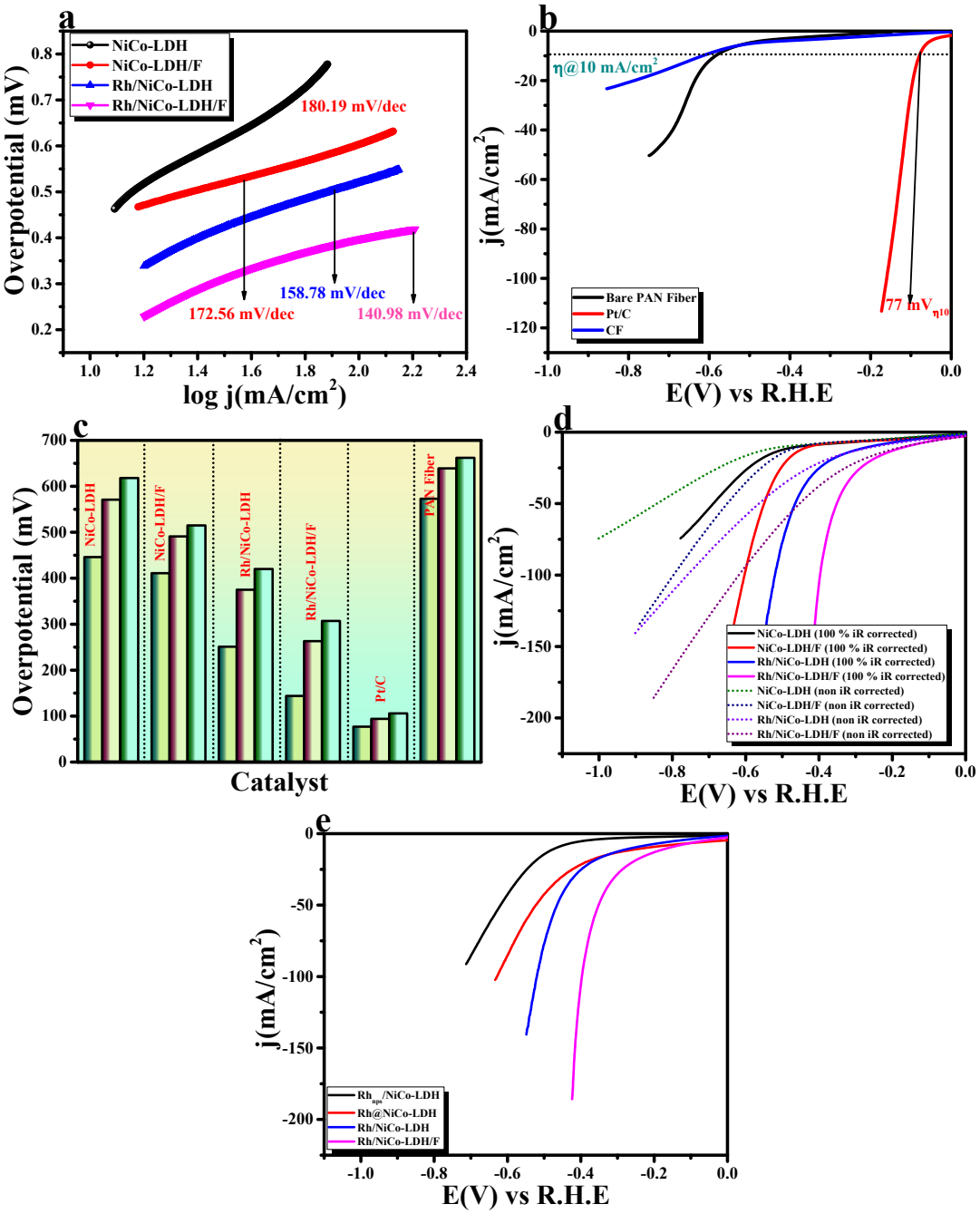

Figure S24. a) Tafel slope of NiCo-LDH, NiCo-LDH/F, Rh/NiCo-LDH, and Rh/NiCo-LDH/F; b) LSV polarization curve of bare PAN fiber, Carbon fiber, and Pt/C; c) bar diagram of overpotential value at different current density; d) LSV polarization iR corrected and non-iR corrected LSV polarization results of NiCo-LDH, NiCo-LDH/F, Rh/NiCo-LDH, and Rh/NiCo-LDH/F; and e) LSV polarization curve of Rh@NiCo-LDH, Rh_{nps}/NiCo-LDH, Rh/NiCo-LDH, and Rh/NiCo-LDH/F.

Table S4. Comparison table of recently reported HER catalysts in alkaline medium. Note: We have compared our material with both powder and fiber materials.

Catalyst	*Substrate*	*Electrolyte*	*Current density*	**Overpotential**	**Reference**
Rh/NiCo-LDH/F	**Carbon Fiber**	**1 M KOH**	**10 mA/cm^2**	**144 mV**	**This work**
$Ni_3Fe(1.33)$@N-C NT/NFs	GCE	1 M KOH	10 mA/cm2	417 mV	[17]
Co-Ni3N nanorods	CC	1 M KOH	10 mA/cm2	194 mV	[18]
Ni/NC catalysts	RDE	1 M KOH	10 mA/cm2	219 mV	[19]
C@NiO/Ni (S2-3%)	GCE	1 M KOH	10 mA/cm2	407 mV	[20]
Co-doped MoS_2 nanofibers	GCE	0.5 M H2SO4	10 mA/cm2	330 mV	[21]
CoS_2@CNFs	GCE	1 M KOH	10 mA/cm2	207 mV	[22]
Co_9S_8@MoS_2/CNFs	GCE	0.5 M H2SO4	10 mA/cm2	190 mV	[23]
Ni_3N/Ni foam	GCE	1 M KOH	10 mA/cm2	257 mV	[24]

Co–WSe_2/MWNTs	GCE	1 M KOH	10 mA/cm2	241 mV	[25]
Mo_2N–Mo_2C/HGr-3	GCE	1 M KOH	10 mA/cm2	154 mV	[26]
$NiFe_2O_4$-NFs	CC	1 M KOH	10 mA/cm2	154 mV	[27]

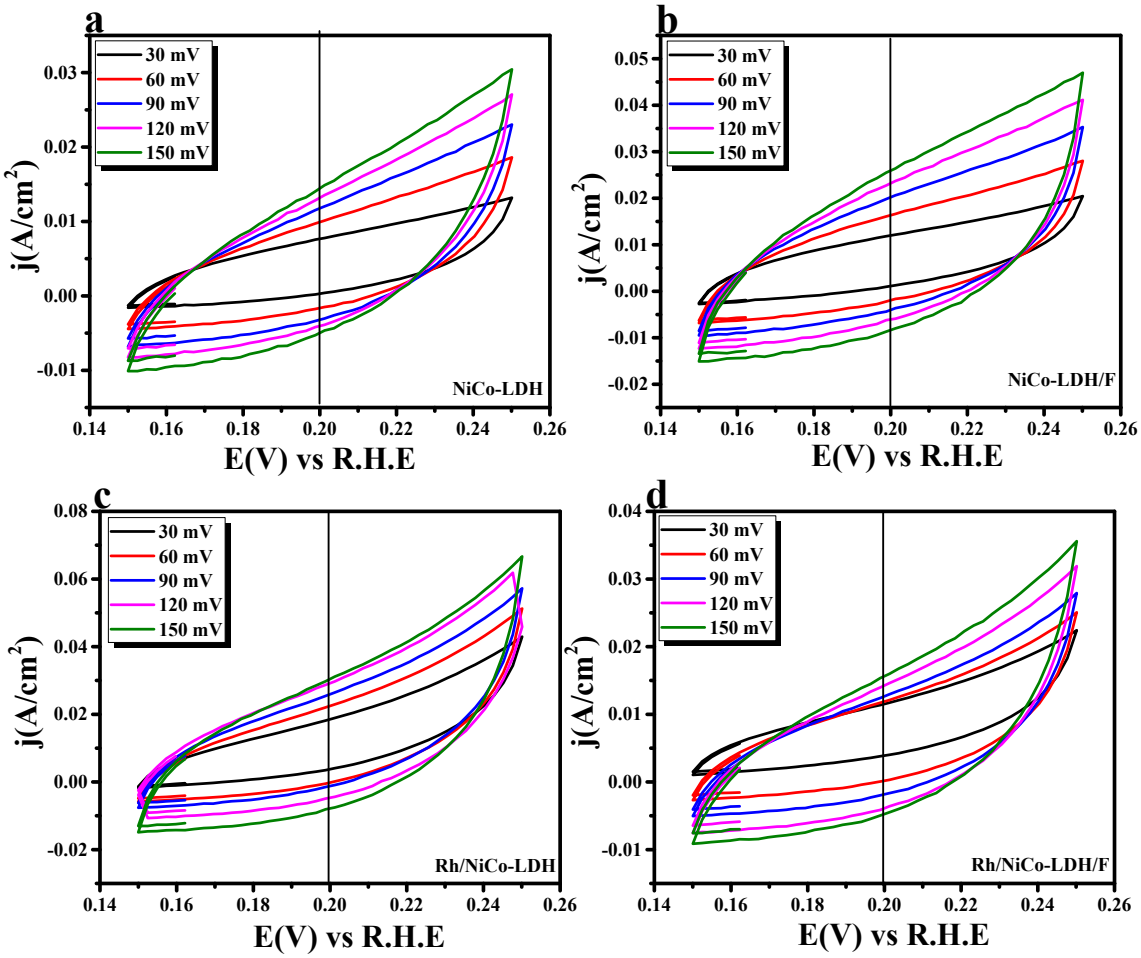

Figure S25. a-d) scan rate-dependent CV curves obtained for calculating the C_{dl} value in the non-faradaic region of 0.15 to 1.25 V vs R.H.E of NiCo-LDH, NiCo-LDH/F, Rh/NiCo-LDH and Rh/NiCo-LDH/F.

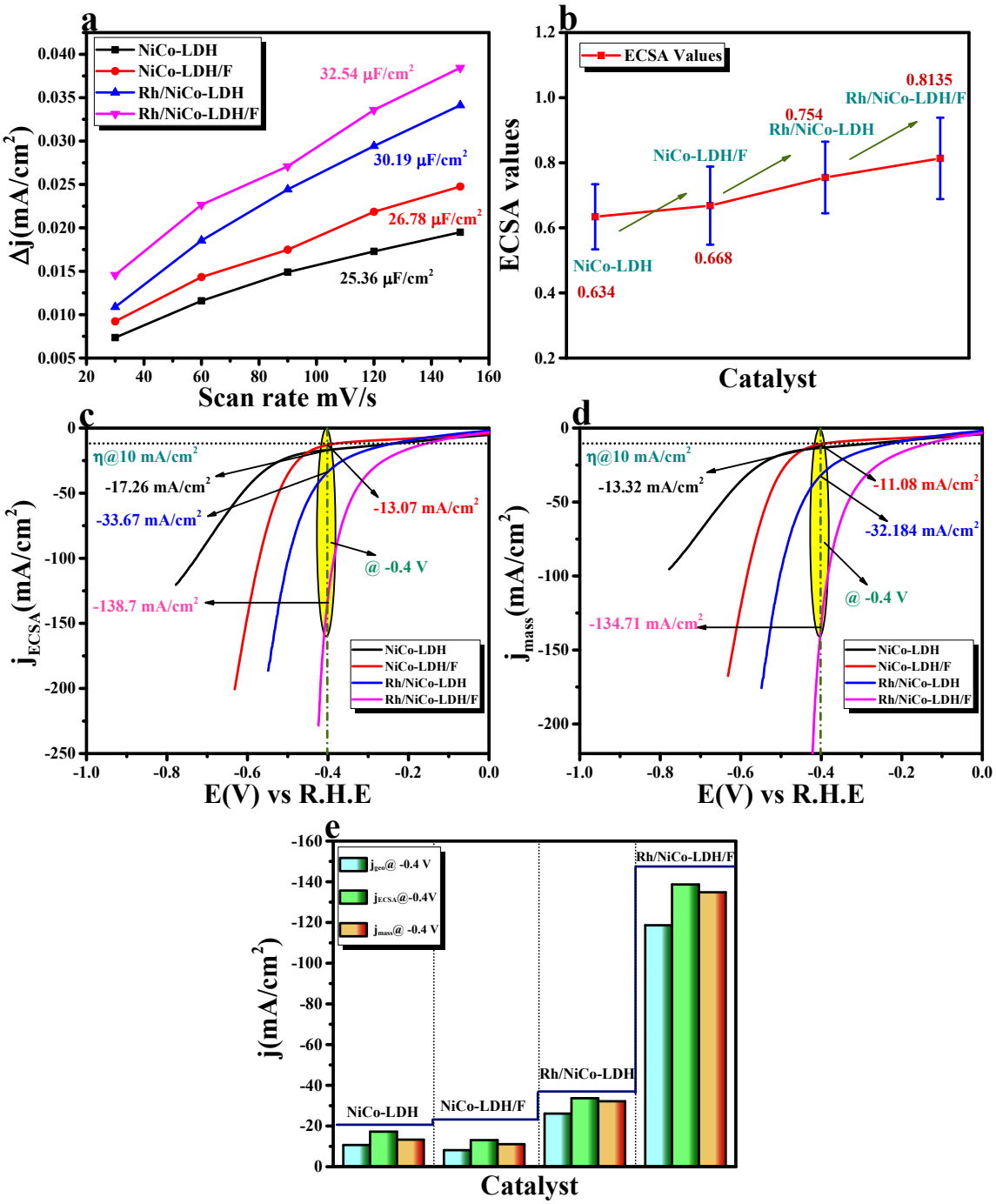

Figure S26. (a) ΔJ vs. scan rate plot for obtaining the C_{dl} information; (b) calculated ECSA; (c) ECSA-normalized LSV polarization curve; (d) mass-normalized LSV polarization curve and (e) current measurement @-0.4 V vs RHE of NiCo-LDH, NiCo-LDH/F, Rh/NiCo-LDH, and Rh/NiCo-LDH/F.

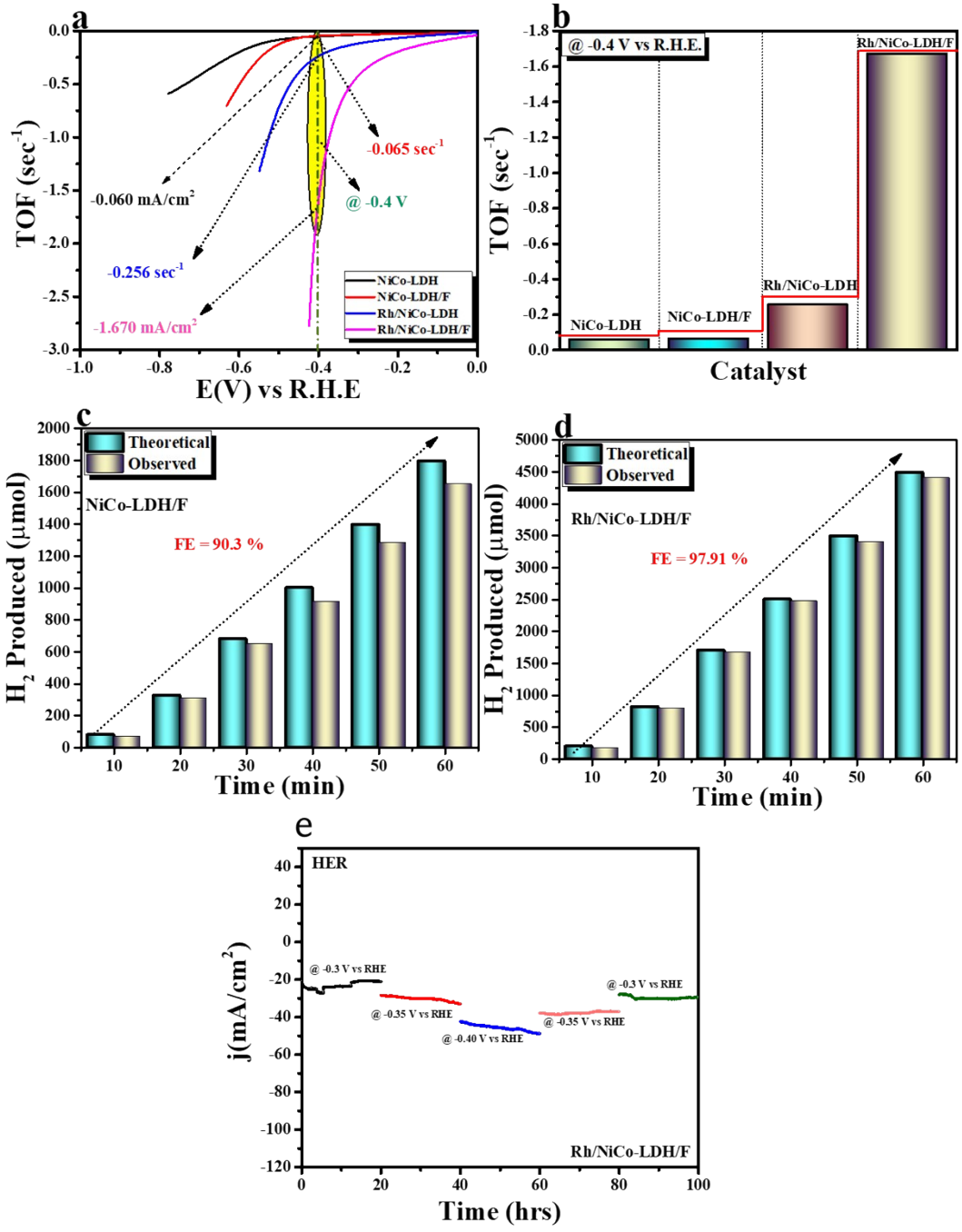

Figure S27. (a) calculated TOF value of NiCo-LDH, NiCo-LDH/F, Rh/NiCo-LDH and Rh/NiCo-LDH/F; b) TOF value @-0.4V of NiCo-LDH, NiCo-LDH/F, Rh/NiCo-LDH and Rh/NiCo-LDH/F; (c-d) Faradaic efficiency and quantitative analysis of produced H_2 in NiCo-LDH/F, Rh/NiCo-LDH/F with different time intervals measured via gas-chromatography and (e) chronoamperometry study of Rh/NiCo-LDH/F at different potential.

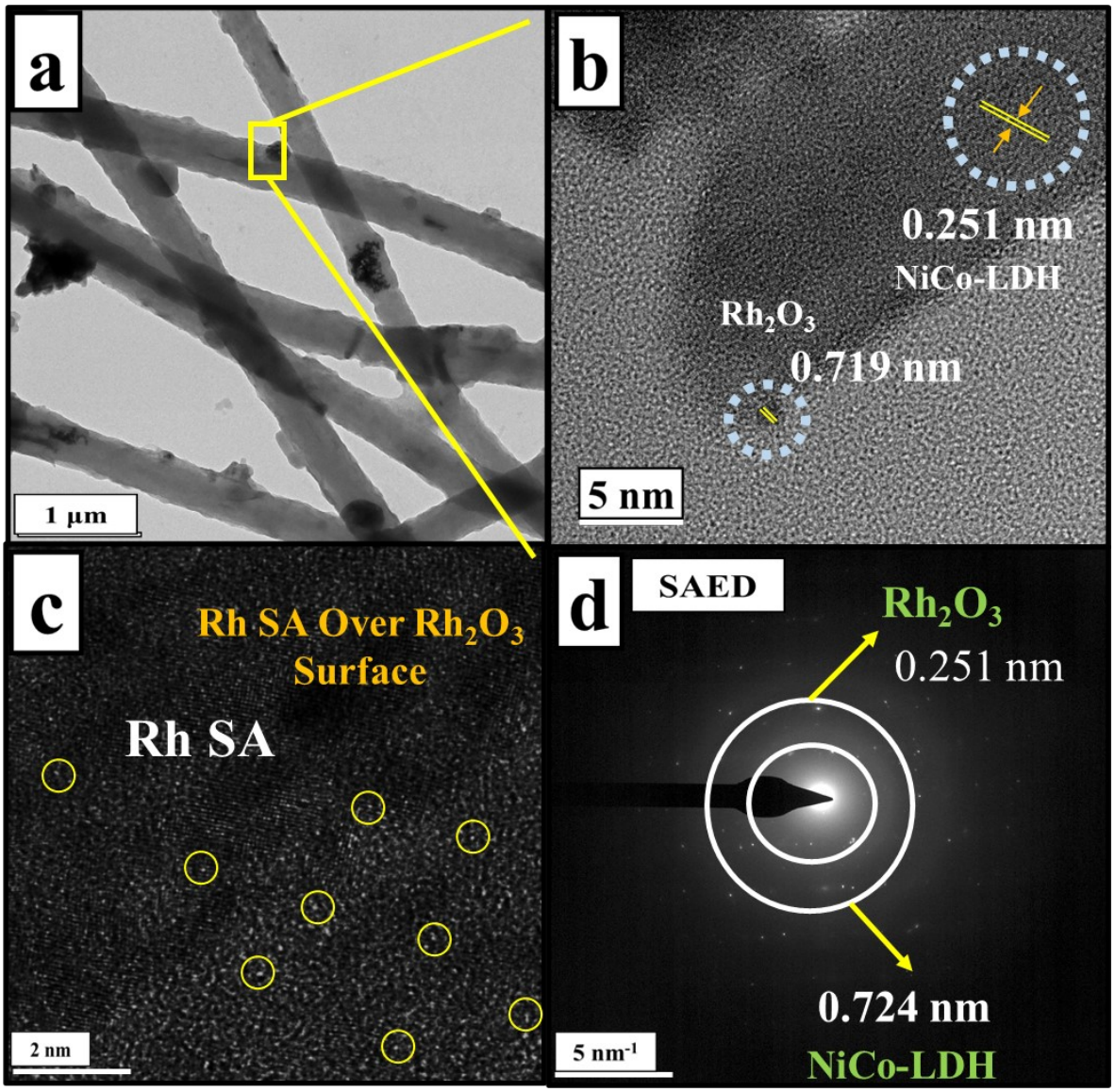

Figure S28. (a) TEM images of post HER-Rh/NiCo-LDH/F; (b) HR-TEM lattice fringes pattern of post HER-Rh/NiCo-LDH/F; (c) AC-STEM images of post-Rh/NiCo-LDH/F; and (d) SAED pattern post HER-Rh/NiCo-LDH/F.

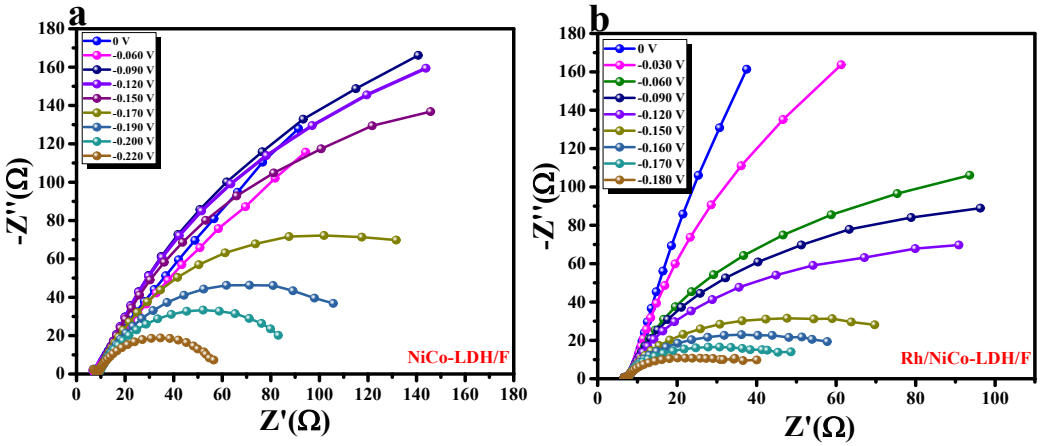

Figure S29. (a,b) Nyquist for NiCo-LDH/F and Rh/NiCo-LDH/F at different applied potentials.

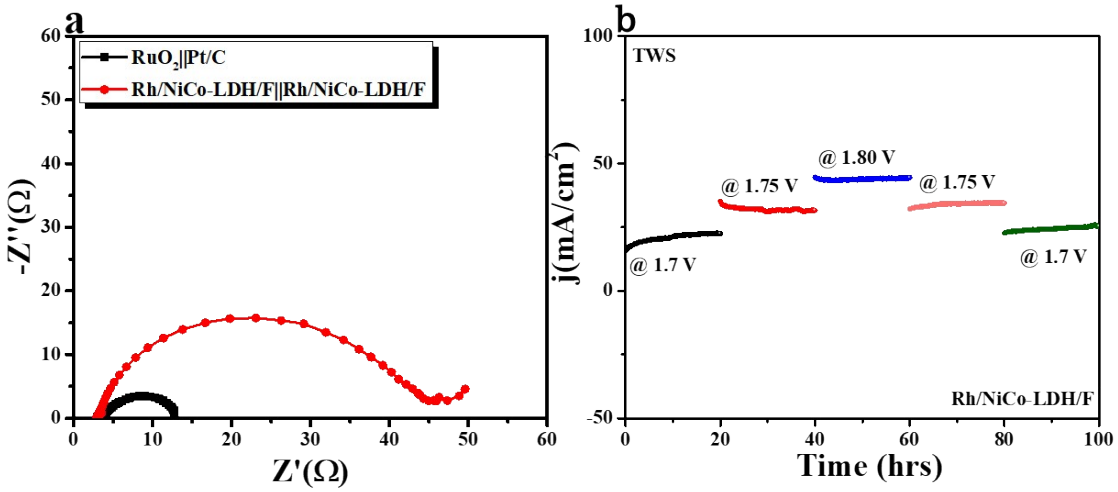

Figure S30. (a) Nyquist plot for Rh/NiCo-LDH/F//Rh/NiCo-LDH/F and RuO_2//Pt/C; b) chronoamperometry study of Rh/NiCo-LDH/F at different potential.

Catalyst	*Substrate*	*Electrolyte*	*Current density*	Cell voltage	Reference
Rh/NiCo-LDH/F	**Carbon Fiber**	**1 M KOH**	**10 mA/cm^2**	**1.63 mV**	**This work**
CoP nano-wires	GCE	1 M KOH	10 mA/cm2	1.63 V	[28]
EG/$Co_{0.85}$Se/NiFe-LDH	GCE	1.0 M KOH	10 mA/cm2	1.67	[29]
Co-PNCNFs	GCE	1.0 M KOH	10 mA/cm2	1.66	[30]
Co-P/NC	RDE	1.0 M KOH	10 mA/cm2	1.71	[31]
CoP/NCF-200/NF	NF	1.0 M KOH	10 mA/cm2	1.64	[32]
CP/CTs/Co-S	graphite plate	1.0 M KOH	10 mA/cm2	1.743	[33]
Ni3S2/NF	NF	1.0 M KOH	10 mA/cm2	1.76	[34]
Ni-N,P/CNFs catalyst	Carbon cloth	1.0 M KOH	10 mA/cm2	1.67	[35]

Table S5. Comparison table of recently reported TWS catalysts in alkaline medium.

Note: We have compared our material with both powder and fiber materials.

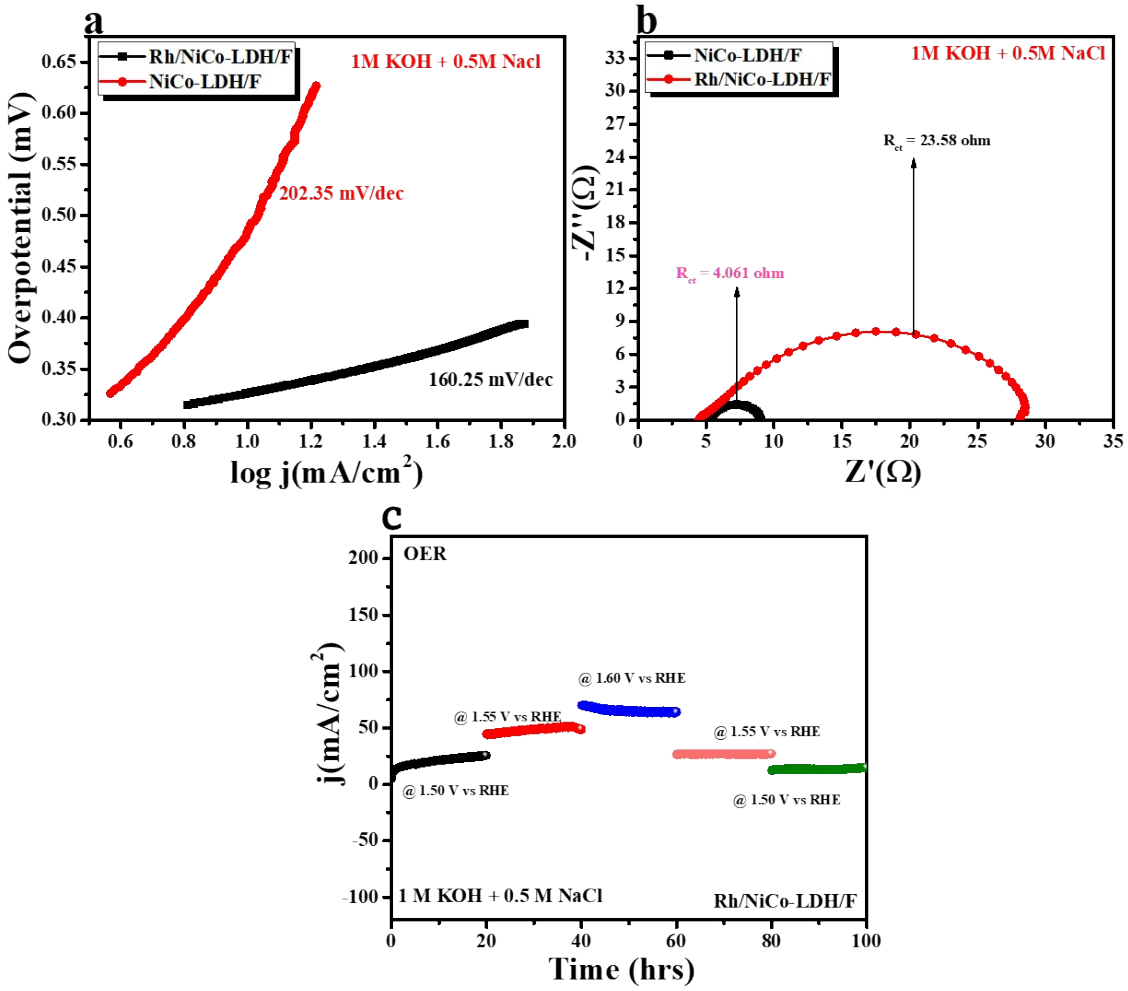

Figure S31. (a-b) Tafel slope and EIS study of Rh/NiCo-LDH/F and NiCo-LDH/F in 1 M KOH + 0.5 M Nacl and b) chronoamperometry study of Rh/NiCo-LDH/F at different potential.

Catalyst	*Substrate*	*Electrolyte*	*Current density*	**Overpotential**	**Reference**
Rh/NiCo-LDH/F	**Carbon Fiber**	**1 M KOH+ 0.5M NaCl**	**10 mA/cm^2**	**307 mV**	**This work**
$NiO/Ni_3S_2@Ni_5P_4/NF$	NF	1.0 M KOH + seawater	10 mA cm^{-2}	310 mV	[36]
Ni_2P-Fe_2P/NF	NF	Alkaline seawater	10 mA cm^{-2}	305 mV	[37]
$Na_2Co_{0.5}Fe_{0.5}P_2O_7$/C	GC electrode	Alkaline seawater	10 mA cm^{-2}	300 mV	[38]
Fe_2O_3-MnO_2	FTO	0.5M KOH + 0.5M NaCl	10 mA cm^{-2}	480 mV	[39]
NiFe-LDH/GC	GC electrode	0.1M KOH + 0.5M NaCl	10 mA cm^{-2}	359 mV	[40]
ER-P/RP-SNCF-5	CC/NF	1M KOH + 0.5M NaCl	10 mA cm^{-2}	332 mV	[41]
Co_3O_4-MnO_2	FTO	0.5M KOH + 0.5M NaCl	10 mA cm^{-2}	450 mV	[39]

Table S6. Comparison table of recently reported OER catalysts in artificial and normal seawater electrolysis. Note: We have compared our material with powder materials.

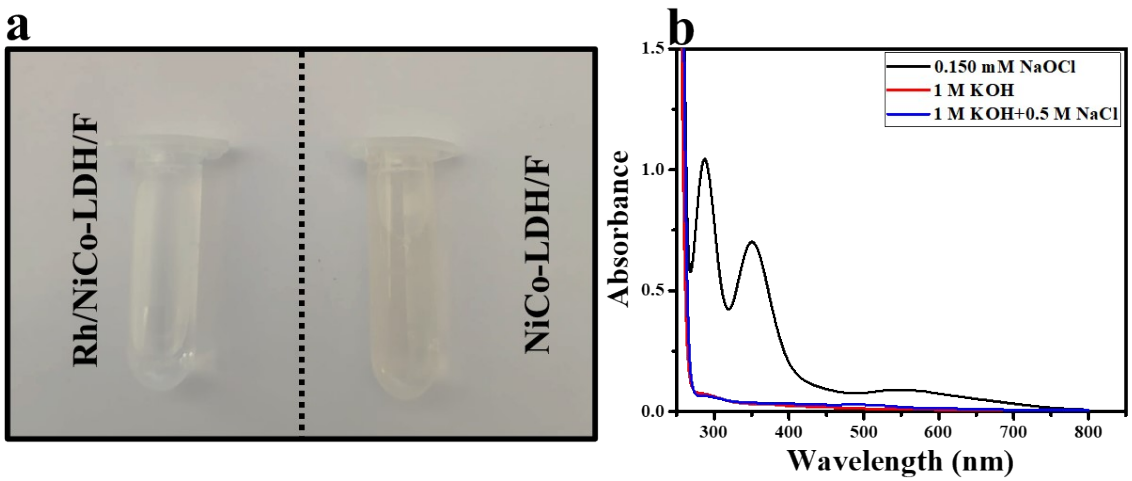

Figure S32. Photos of electrolytes (1 M KOH + 0.5 M NaCl) for Rh/NiCo-LDH/F and NiCo-LDH/F after chronoamperometric test under potentials to deliver a current density of 50 mA/cm^2 and The UV–vis absorption spectra of the Rh/NiCo-LDH from 1.0 M KOH and 1.0 M KOH + 0.5 M NaCl after anodic oxidation.

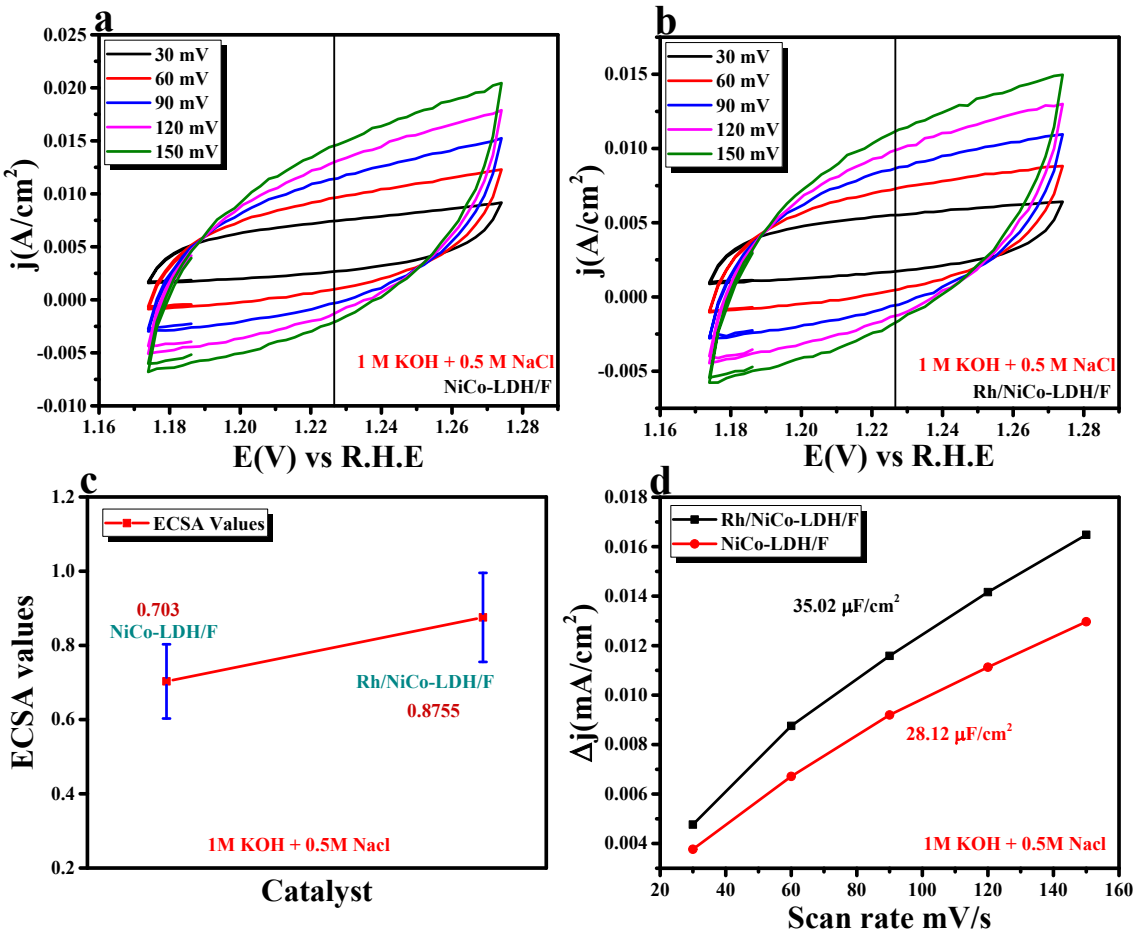

Figure S33. (a-b) Scan rate-dependent CV curves obtained for calculating the C_{dl} value in the non-faradaic region for NiCo-LDH/F and Rh/NiCo-LDH/F in 1 M KOH + 0.5 M NaCl; (c) calculated ECSA; and (d) ΔJ vs. scan rate plot for obtaining the C_{dl} information for NiCo-LDH/F and Rh/NiCo-LDH/F in in 1 M KOH + 0.5 M NaCl.

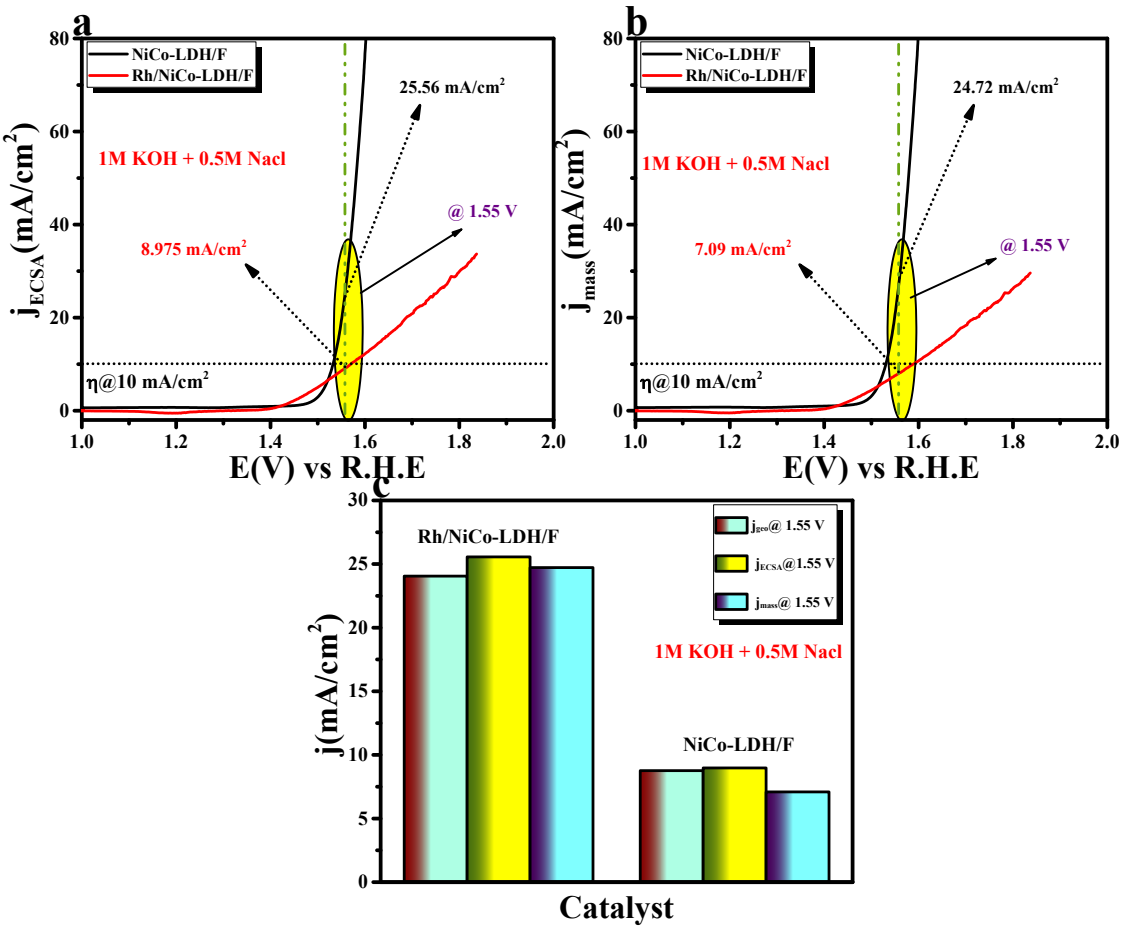

Figure S34. (a-b) ECSA and Mass normalized LSV polarization curve of NiCo-LDH/F and Rh/NiCo-LDH/F in 1 M KOH + 0.5 M NaCl and (c) current measurement at 1.55 V vs RHE from geometrical, ECSA and Mass normalization LSV studies for NiCo-LDH/F and Rh/NiCo-LDH/F in 1 M KOH + 0.5 M NaCl.

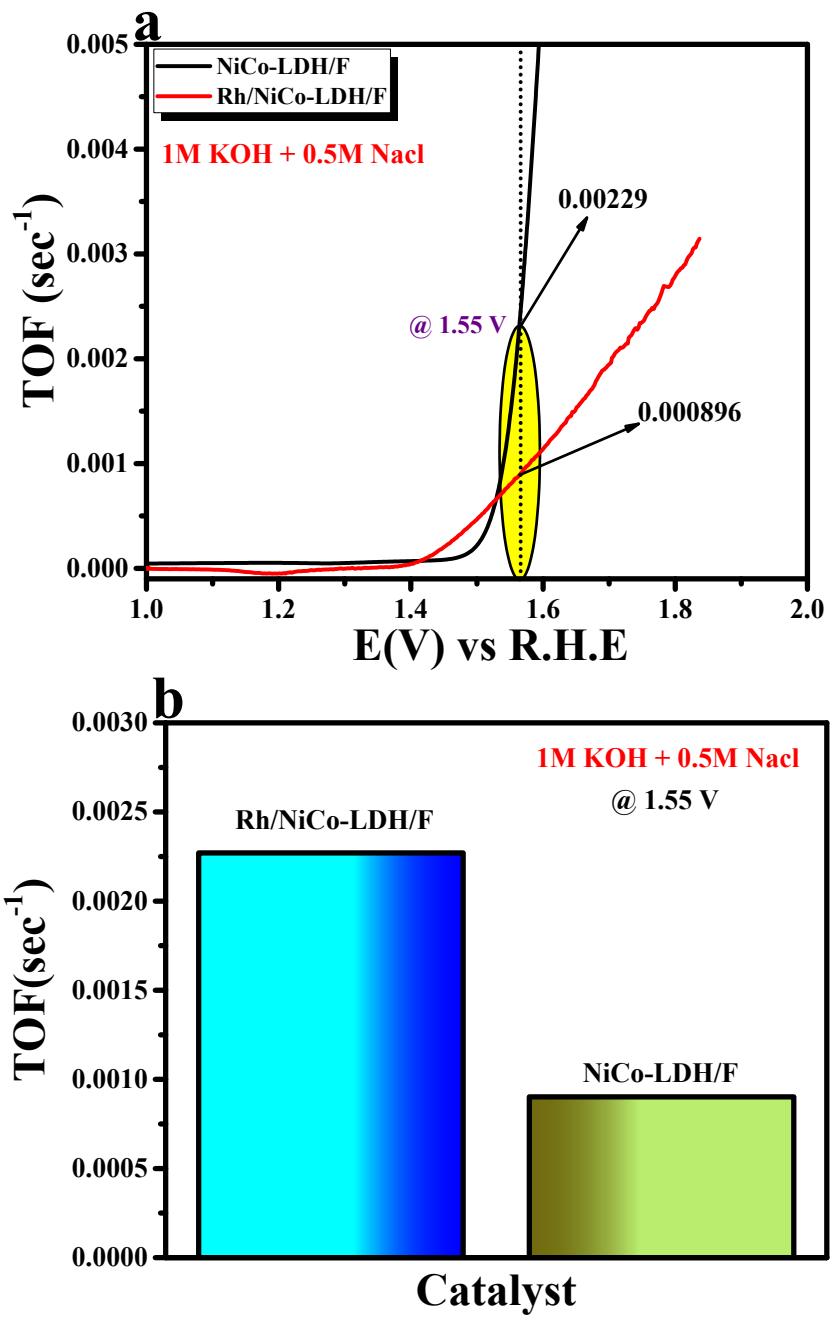

Figure S35. (a) calculated TOF value of NiCo-LDH/F and Rh/NiCo-LDH/F; and (b) TOF value @1.55V of NiCo-LDH/F, and Rh/NiCo-LDH/F.

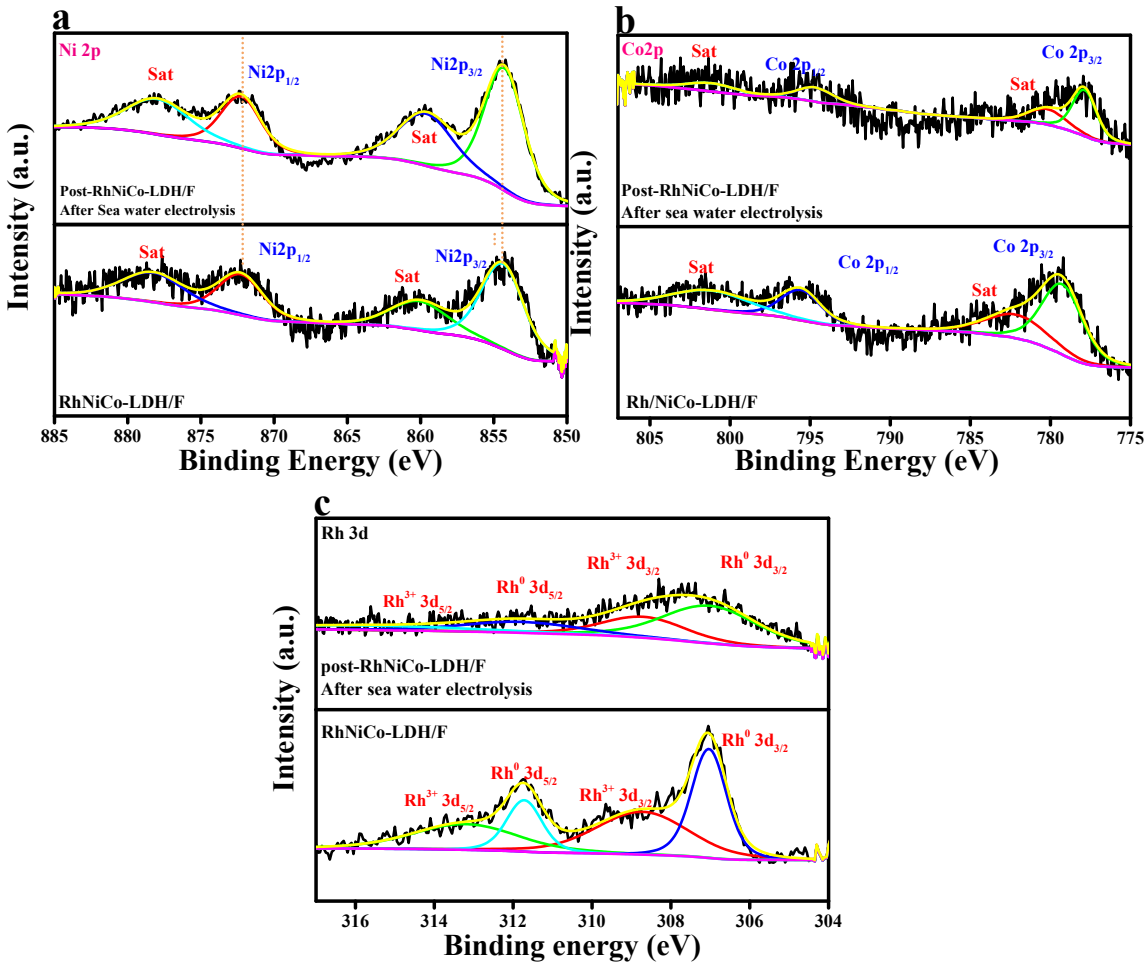

Figure S36. Post XPS: (a-c) deconvolved XPS spectrum of Ni 2p; deconvolved XPS spectrum of Co 2p and deconvolved XPS spectrum of Rh 3d for post OER-after seawater electrolysis.

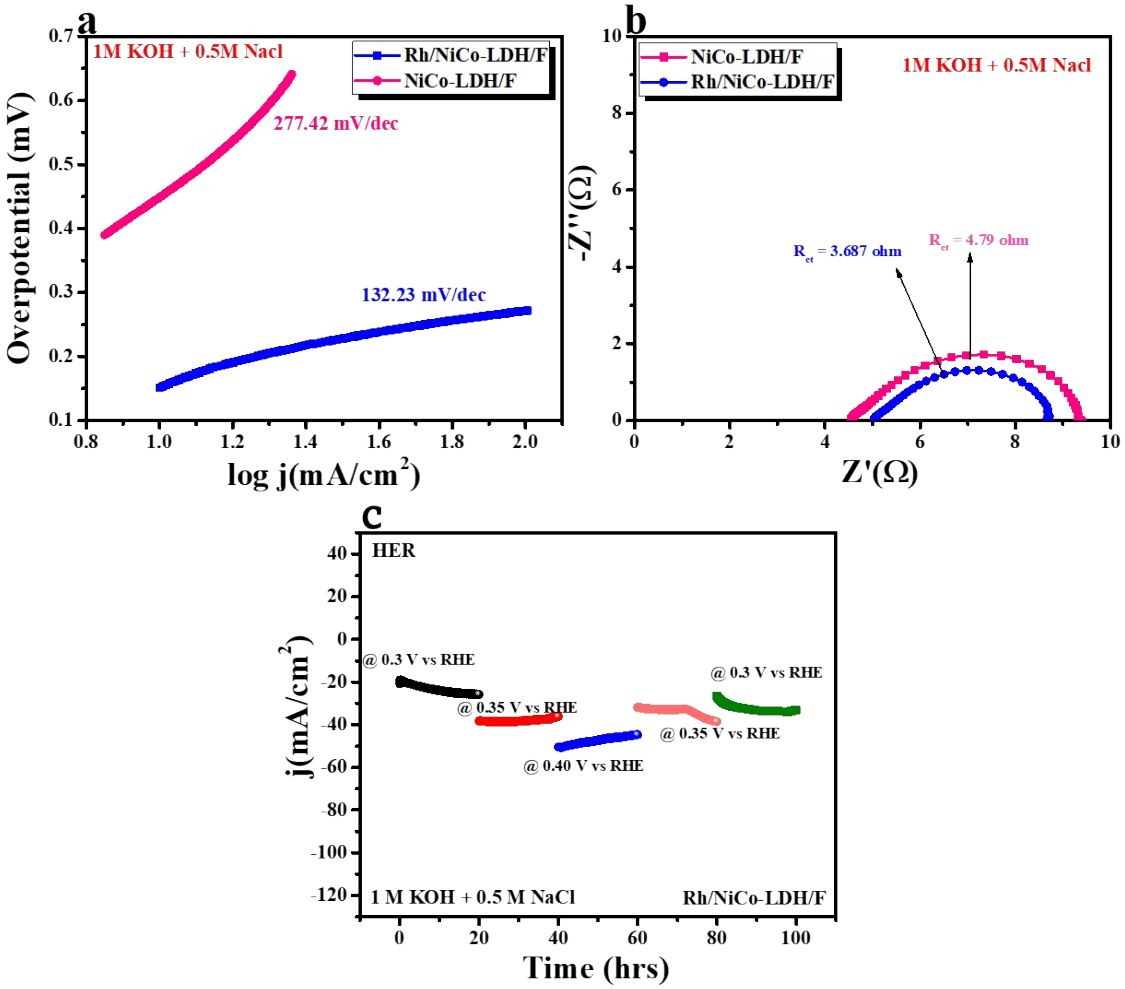

Figure S37. (a-b) Tafel slope and EIS study of Rh/NiCo-LDH/F and NiCo-LDH/F in 1 M KOH + 0.5 M Nacl and b) chronoamperometry study of Rh/NiCo-LDH/F at different potential.

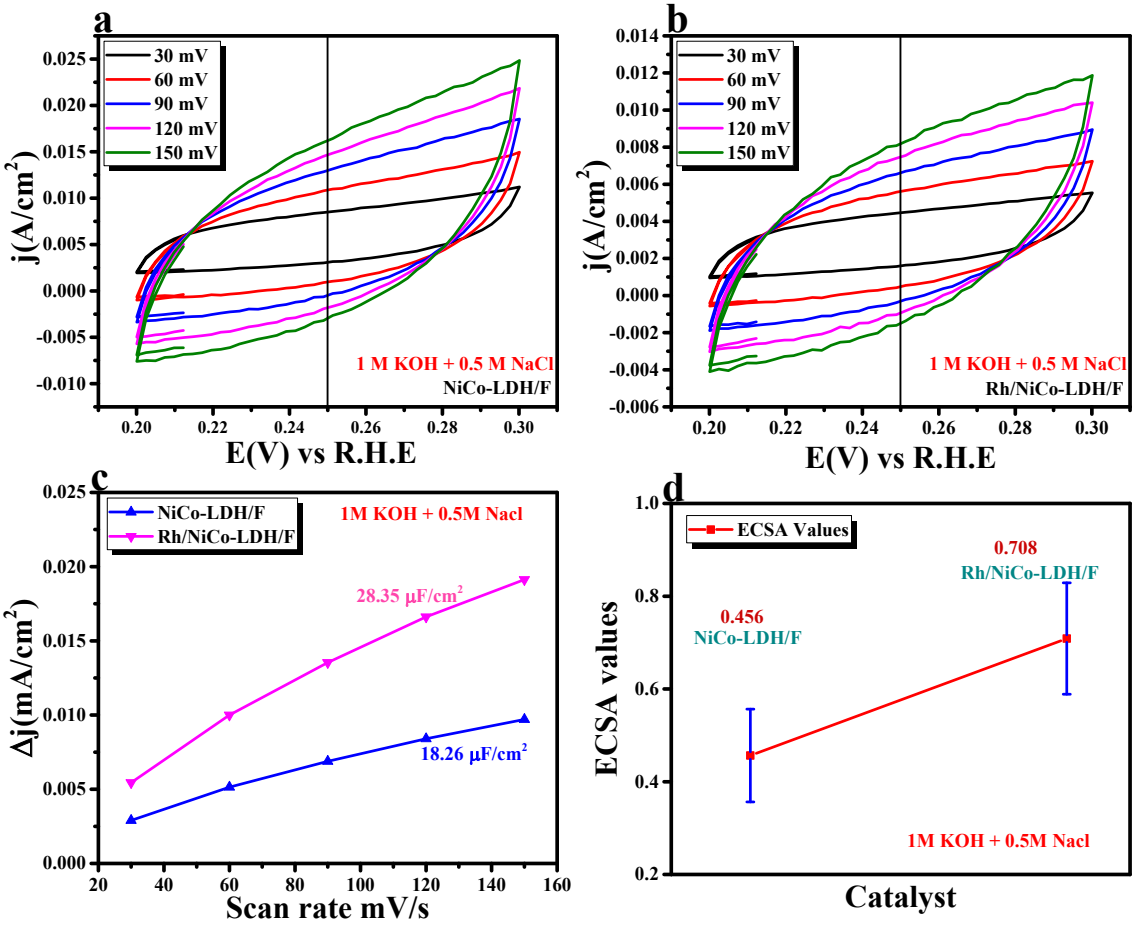

Figure S38. HER performance in 1 M KOH + 0.5 M NaCl; (a-b) Scan rate-dependent CV curves obtained for calculating the C_{dl} value in the non-faradaic region for NiCo-LDH/F and Rh/NiCo-LDH/F in 1 M KOH + 0.5 M NaCl; (c) calculated ECSA; and d) ΔJ vs. scan rate plot for obtaining the C_{dl} information for NiCo-LDH/F and Rh/NiCo-LDH/F in in 1 M KOH + 0.5 M NaCl.

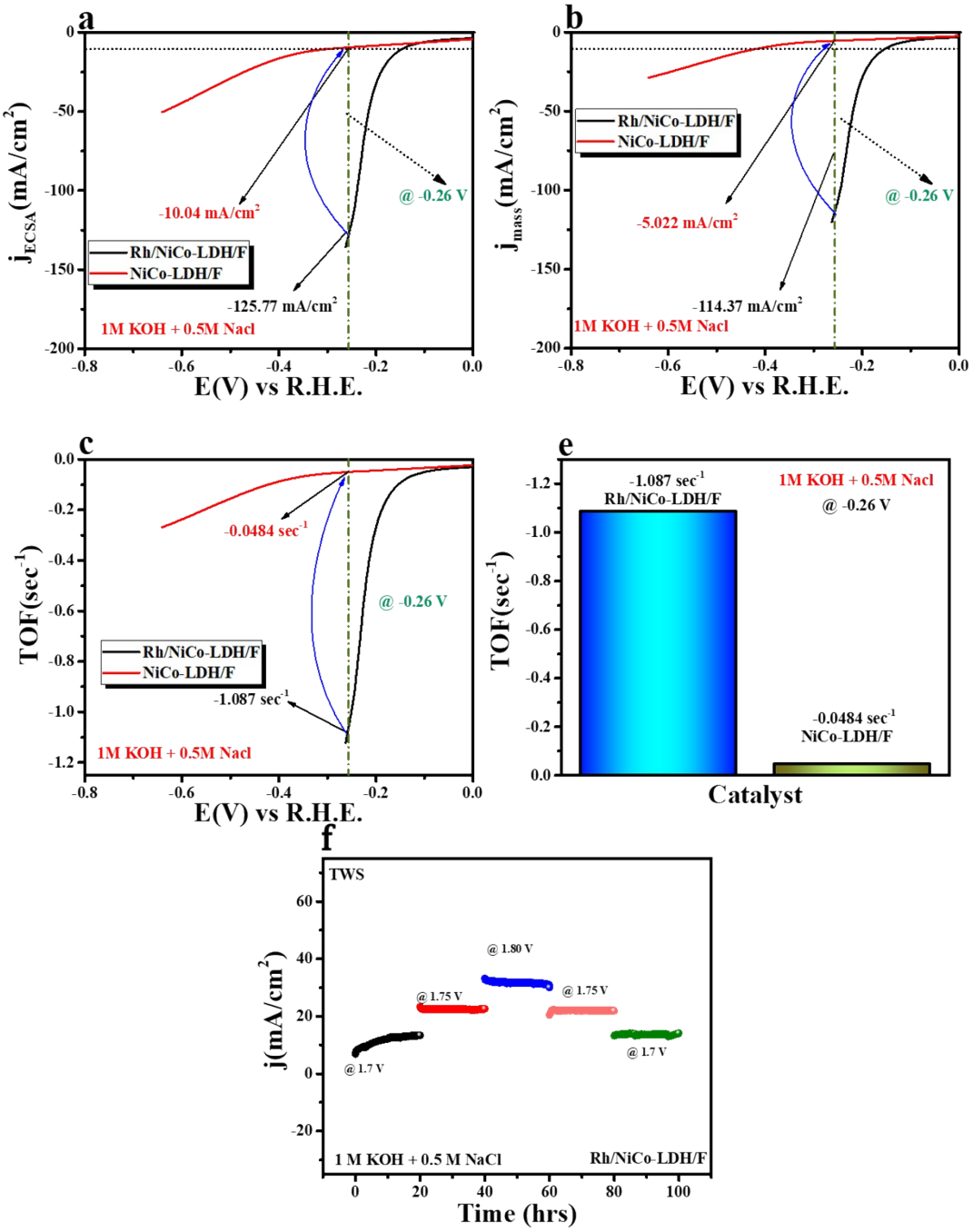

Figure S39. HER performance in 1 M KOH + 0.5 M NaCl; (a-b) ECSA and Mass normalized LSV polarization curve of NiCo-LDH/F and Rh/NiCo-LDH/F in 1 M KOH + 0.5 M NaCl and (c) calculated TOF value of NiCo-LDH/F and Rh/NiCo-LDH/F; and d) TOF value @1.55V of NiCo-LDH/F, and Rh/NiCo-LDH/F and (f) chronoamperometry study of Rh/NiCo-LDH/F at different potential.

Catalyst	*Substrate*	*Electrolyte*	*Current density*	**Overpotential**	**Reference**
Rh/NiCo-LDH/F	**Carbon Fiber**	**1 M KOH+ 0.5M NaCl**	**10 mA/cm²**	**167 mV**	**This work**
Ni_2P-Fe_2P/NF	NF	Alkaline seawater	10 mA cm^{-2}	252 mV	[37]
CoNiP/Co_xP	NF	Seawater	10 mA cm^{-2}	290 mV	[42]
NP-MoS_2/CC	CC	Alkaline seawater	10 mA cm^{-2}	354.4 mV	[43]
NiFe LDH/FeOOH	INF	1 M KOH + 0.5 M NaCl	10 mA cm^{-2}	181.8 mV	[44]
$Cu_{0.98}La_{0.02}O$ (CS)	Stainless steel	1 m KOH + 1 m NaCl	10 mA cm^{-2}	410 mV	[45]
Ni-SA/NC	Pluronic F127	Alkaline seawater	100 mA cm^{-2}	305 mV	[46]

Table S7. Comparison table of recently reported HER catalysts in artificial and normal seawater electrolysis. Note: We have compared our material with powder materials.

Catalyst	*Substrate*	*Electrolyte*	*Current density*	**Cell Voltage**	**Reference**
Rh/NiCo-LDH/F	**Carbon Fiber**	**1 M KOH+ 0.5M NaCl**	**10 mA/cm²**	**167 mV**	**This work**
MoN–Co_2N NSs	GC	Alkaline seawater	10 mA cm^{-2}	1.70 V	[47]
CoPx@FeOOH	NF	1.0 M KOH Seawater	100 mA cm^{-2}	1.71	[48]
$CoSe_2$–NCF	CC	Alkaline seawater	10 mA cm^{-2}	1.84 V	[49]
Ni-Fe-Mo//Ni-Fe-Mo	Graphitic carbon felt	Alkaline seawater	10 mA cm^{-2}	1.68 V	[50]
Ce–NiFe LDH/NF	NF	Alkaline seawater	10 mA cm^{-2}	1.81 V	[51]

Table S8. Comparison table of recently reported TWS catalysts in artificial and normal seawater electrolysis. Note: We have compared our material with powder materials.

Computational Details:

The Vienna ab initio Simulation Package (VASP), which is based on plane wave basis sets with projector-augmented wave (PAW) pseudopotential were used for all spin polarized DFT calculation in this work.[1-3] The exchange correlation functional Perdew-Burke-Ernzerhof (PBE) was utilized at the level of Generalized Gradient Approximation (GGA).[4] For all the calculations, the dispersion correction term was considered using the van der Waal density correction by IVDW=11 tag.[5] Throughout the computations, the 500 eV kinetic energy cut off for the plane wave expansion were employed. During geometries optimization, along the z-axis more than 21 Å were used to build the vacuum space. For optimization, the gamma packed grid of 1x1x1 is employed to sample the Brillouin zone. A threshold of 10^{-5} eV total energy was used to converge the electronic density. In the same way, less than of 0.01 eV/Å maximum force on any ion is employed for the structure optimization. After the geometry optimizations, the density of state calculations were performed using the LORBIT=11 tag.[6] For analysis the results, the VASPKIT tool was used. Another type of crucial calculation Crystal orbital Hamilton Population (COHP) were employed to understanding the bonding strength. For the visualizations, LOBSTER software is used.[7,8] The transition state energy barrier between the intermediate states were determined using the Henkelman group's climbing image-nudged elastic band method.[9,10,52–55]

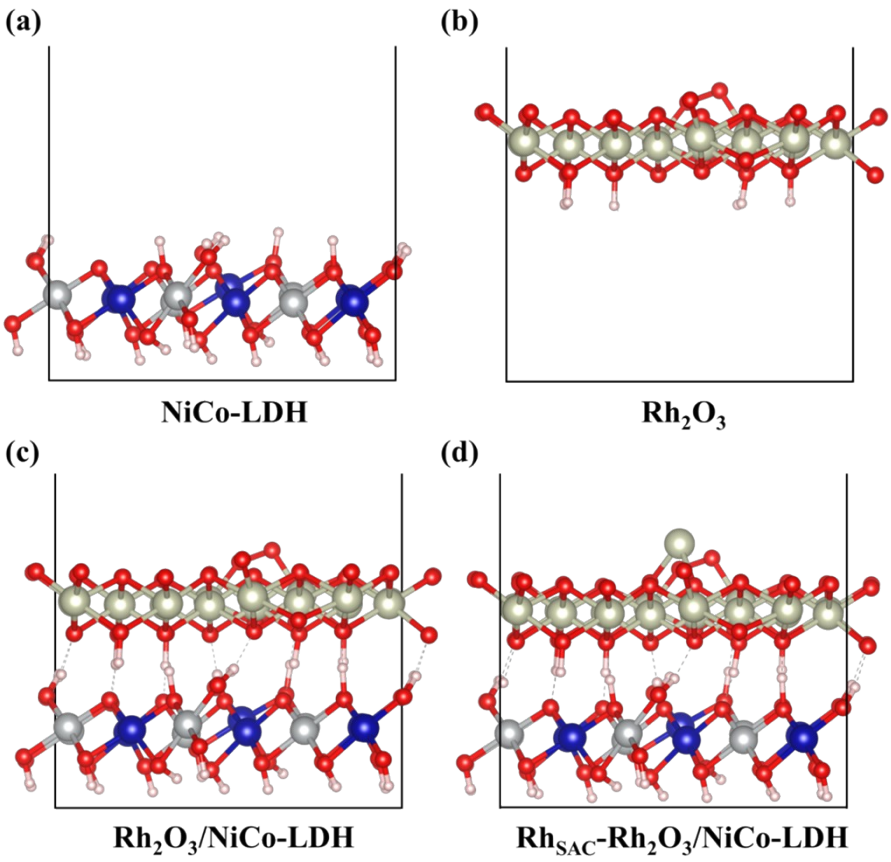

Figure S40: Optimized structure for Side view of (a) NiCo LDH (b) Rh_2O_3 (c) Rh_2O_3/NiCo LDH and (d) Rh-Rh_2O_3/NiCo LDH.

(a) Model clarification:

We would like to clarify that the model used in this study represents a **Rh_2O_3/NiCo-LDH heterojunction**, rather than a simple Rh-doped system. To better reflect the experimental system, we constructed a heterostructure model consisting of Rh_2O_3 interfaced with NiCo-LDH, along with an isolated Rh metal site located at the heterointerface (denoted as Rh–Rh_2O_3/NiCo-LDH). The DFT results indicate that the Rh site at the heterointerface plays a crucial role in enhancing the OER activity, thereby supporting the synergistic effect of the heterojunction. To avoid any

ambiguity, we have now included detailed structural representations of all optimized models in the revised manuscript including NiCo-LDH, Rh_2O_3, Rh_2O_3/NiCo-LDH, and Rh–Rh_2O_3/NiCo-LDH.

(b) Hubbard U and spin treatment:

We appreciate the reviewer's comment regarding the Hubbard U correction. We acknowledge that the choice of U for Ni/Co 3d electrons is highly sensitive to the spin state and local coordination environment, and requires careful benchmarking. To avoid introducing uncertainty from arbitrarily chosen U values, we did not apply a Hubbard U correction in the present study. Instead, all calculations were performed using **spin-polarized settings (ISPIN = 2)**, allowing the system to converge to the most energetically favorable spin configuration. This clarification has now been added to the revised Computational Details section.

(c) Slab model and convergence parameters:

We thank the reviewer for pointing out the need for explicit computational details. In our calculations, a slab thickness of approximately **9 Å** was used, along with a vacuum spacing of more than **21 Å** along the z-axis to avoid spurious interactions between periodic images. The convergence criteria were set to $\mathbf{10^{-5}}$ **eV** for total energy and **0.01 eV** $\mathbf{Å^{-1}}$ for the maximum force on each atom.

	Optimized Structure		Bind_O		Bind_OOH	
	Rh Charge	NiCo LDH surface Charge Transfer to Rh_{SAC}-Rh_2O_3-NiCo surface	Rh Charge	System Charge Transfer to O	Rh Charge	System Charge Transfer to OOH
Rh_{SAC}-Rh_2O_3-NiCo surface	+0.785e	-0.3255e	1.224386e	1.041839e	1.079046e	0.676615e
NiCo LDH surface			1.195797e	1.973218e	1.205596e	2.820378e

Table S9: Bader charge values for Rh/NiCo-LDh and NiCo-LDH.

References

1 A. Karmakar, K. Karthick, S. S. Sankar, S. Kumaravel, R. Madhu, K. Bera, H. N. Dhandapani, S. Nagappan, P. Murugan and S. Kundu, *Journal of Materials Chemistry A*, 2022, **10**, 3618–3632.

2 Y. Yang, Q.-N. Yang, Y.-B. Yang, P.-F. Guo, W.-X. Feng, Y. Jia, K. Wang, W.-T. Wang, Z.-H. He and Z.-T. Liu, *ACS Catalysis*, 2023, **13**, 2771–2779.

3 S. Singha Roy, R. Madhu, K. Bera, S. Nagappan, H. N. Dhandapani, A. De and S. Kundu, *ACS Applied Materials & Interfaces*, 2024, **16**, 5965–5976.

4 Y. Song, J. Cheng, J. Liu, Q. Ye, X. Gao, J. Lu and Y. Cheng, *Applied Catalysis B: Environmental*, 2021, **298**, 120488.

5 B. Qiu, L. Cai, Y. Wang, Z. Lin, Y. Zuo, M. Wang and Y. Chai, *Advanced Functional Materials*, DOI:10.1002/adfm.201706008.

6 W. Li, L. Zhao, C. Wang, X. Lu and W. Chen, *ACS Applied Materials & Interfaces*, 2021, **13**, 46998–47009.

7 Z. Zhang, J. Zhang, T. Wang, Z. Li, G. Yang, H. Bian, J. Li and D. Gao, *RSC Advances*, 2018, **8**, 5338–5343.

8 W. Zong, D. Rao, H. Guo, Y. Ouyang, Y.-E. Miao, W. Wang, J. Wang, F. Lai and T. Liu, *Nanoscale*, 2020, **12**, 10977–10986.

9 Z. Zhang, X. Liang, J. Li, J. Qian, Y. Liu, S. Yang, Y. Wang, D. Gao and D. Xue, *ACS Applied Materials & Interfaces*, 2020, **12**, 21661–21669.

10 M. Sreenivasulu, A. Hadrihalli, M. A. Alshehri and N. P. Shetti, *Energy & Fuels*, 2024, **38**, 12888–12899.

11 X. Liang, Y. Li, H. Fan, S. Deng, X. Zhao, M. Chen, G. Pan, Q. Xiong and X. Xia, *Nanotechnology*, 2019, **30**, 484001.

12 L. Yang, L. Chen, D. Yang, X. Yu, H. Xue and L. Feng, *Journal of Power Sources*, 2018, **392**, 23–32.

13 Z. Zhang, J. Zhou, H. Wei, Y. Dai, S. Li, H. Shi and G. Xu, *Journal of Materials Science*, 2020, **55**, 16625–16640.

14 B. Chen, Z. Zhang, S. Kim, S. Lee, J. Lee, W. Kim and K. Yong, *ACS Applied Materials & Interfaces*, 2018, **10**, 44518–44526.

15 X. Zhang, A. N. Marianov, Y. Jiang, C. Cazorla and D. Chu, *ACS Applied Nano Materials*, 2020, **3**, 887–895.

16 J. Yu, R. Fu, S. Ge, C. Yang, Y. Zhao, C. Feng, Q. Jiao and H. Li, *New Journal of Chemistry*, 2024, **48**, 6625–6632.

17 T. Li, G. Luo, K. Liu, X. Li, D. Sun, L. Xu, Y. Li and Y. Tang, *Advanced Functional Materials*, DOI:10.1002/adfm.201805828.

18 C. Zhu, A. Wang, W. Xiao, D. Chao, X. Zhang, N. H. Tiep, S. Chen, J. Kang, X. Wang, J. Ding, J. Wang, H. Zhang and H. J. Fan, *Advanced Materials*, DOI:10.1002/adma.201705516.

19 X. Zhang, H. Xu, X. Li, Y. Li, T. Yang and Y. Liang, *ACS Catalysis*, 2016, **6**, 580–588.

20 A. Chinnappan, J. Dongxiao, W. A. D. M. Jayathilaka, C. Baskar, X. Qin and S. Ramakrishna, *International Journal of Hydrogen Energy*, 2018, **43**, 15217–15224.

21 Y. Rheem, S. H. Park, Y. Han, K.-H. Lee, S.-M. Choi and N. V. Myung, *Journal of The Electrochemical Society*, 2019, **166**, F996–F999.

22 H. Gu, Y. Huang, L. Zuo, W. Fan and T. Liu, *Inorganic Chemistry Frontiers*, 2016, **3**, 1280–1288.

23 H. Zhu, L. Gu, D. Yu, Y. Sun, M. Wan, M. Zhang, L. Wang, L. Wang, W. Wu, J. Yao, M. Du and S. Guo, *Energy & Environmental Science*, 2017, **10**, 321–330.

24 J. Jiang, M. Gao, W. Sheng and Y. Yan, *Angewandte Chemie*, 2016, **128**, 15466–15471.

25 G. Zhang, X. Zheng, Q. Xu, J. Zhang, W. Liu and J. Chen, *Journal of Materials Chemistry A*, 2018, **6**, 4793–4800.

26 H. Yan, Y. Xie, Y. Jiao, A. Wu, C. Tian, X. Zhang, L. Wang and H. Fu, *Advanced Materials*, DOI:10.1002/adma.201704156.

27 S. S. Selvasundarasekar, T. K. Bijoy, S. Kumaravel, A. Karmakar, R. Madhu, K. Bera, S. Nagappan, H. N. Dhandapani, S.-C. Lee and S. Kundu, *Nanoscale*, 2022, **14**, 10360–10374.

28 M. Zhang, S. Ci, H. Li, P. Cai, H. Xu and Z. Wen, *International Journal of Hydrogen Energy*, 2017, **42**, 29080–29090.

29 Y. Hou, M. R. Lohe, J. Zhang, S. Liu, X. Zhuang and X. Feng, *Energy & Environmental Science*, 2016, **9**, 478–483.

30 Y. Zhao, J. Zhang, K. Li, Z. Ao, C. Wang, H. Liu, K. Sun and G. Wang, *Journal of Materials Chemistry A*, 2016, **4**, 12818–12824.

31 B. You, N. Jiang, M. Sheng, S. Gul, J. Yano and Y. Sun, *Chemistry of Materials*, 2015, **27**, 7636–7642.

32 J. Tong, Y. Li, L. Bo, W. Li, T. Li, Q. Zhang, D. Kong, H. Wang and C. Li, *ACS Sustainable Chemistry & Engineering*, 2019, **7**, 17432–17442.

33 J. Wang, H. Zhong, Z. Wang, F. Meng and X. Zhang, *ACS Nano*, 2016, **10**, 2342–2348.

34 L.-L. Feng, G. Yu, Y. Wu, G.-D. Li, H. Li, Y. Sun, T. Asefa, W. Chen and X. Zou, *Journal of the American Chemical Society*, 2015, **137**, 14023–14026.

35 J. Yu, J. Li, C.-Y. Xu, Q. Li, Q. Liu, J. Liu, R. Chen, J. Zhu and J. Wang, *Nano Energy*, 2022, **98**, 107266.

36 Y. Yu, X. Chen, J. Li, Y. Xiao, X. Shi, P. Rao, P. Deng, H. Wen and X. Tian, *International Journal of Hydrogen Energy*, 2024, **51**, 1373–1380.

37 L. Wu, L. Yu, F. Zhang, B. McElhenny, D. Luo, A. Karim, S. Chen and Z. Ren, *Advanced Functional Materials*, DOI:10.1002/adfm.202006484.

38 H. J. Song, H. Yoon, B. Ju, D.-Y. Lee and D.-W. Kim, *ACS Catalysis*, 2020, **10**, 702–709.

39 L. Bigiani, D. Barreca, A. Gasparotto, T. Andreu, J. Verbeeck, C. Sada, E. Modin, O. I. Lebedev, J. R. Morante and C. Maccato, *Applied Catalysis B: Environmental*, 2021, **284**, 119684.

40 F. Dionigi, T. Reier, Z. Pawolek, M. Gliech and P. Strasser, *ChemSusChem*, 2016, **9**, 962–972.

41 F. Liu, R. Hu, H. Qiu, H. Miao, Q. Wang and J. Yuan, *Journal of Alloys and Compounds*, 2022, **913**, 165342.

42 D. Liu, H. Ai, M. Chen, P. Zhou, B. Li, D. Liu, X. Du, K. H. Lo, K. Ng, S. Wang, S. Chen, G. Xing, J. Hu and H. Pan, *Small*, DOI:10.1002/smll.202007557.

43 K. Sun, L. Zeng, S. Liu, L. Zhao, H. Zhu, J. Zhao, Z. Liu, D. Cao, Y. Hou, Y. Liu, Y. Pan and C. Liu, *Nano Energy*, 2019, **58**, 862–869.

44 K. Jiang, W. Liu, W. Lai, M. Wang, Q. Li, Z. Wang, J. Yuan, Y. Deng, J. Bao and H. Ji, *Inorganic Chemistry*, 2021, **60**, 17371–17378.

45 J. D. Rodney, S. Deepapriya, M. C. Robinson, S. J. Das, S. Perumal, P. Sivakumar, H. Jung, B. C. Kim and C. J. Raj, *Applied Materials Today*, 2021, **24**, 101079.

46 W. Zang, T. Sun, T. Yang, S. Xi, M. Waqar, Z. Kou, Z. Lyu, Y. P. Feng, J. Wang and S. J. Pennycook, *Advanced Materials*, DOI:10.1002/adma.202003846.

47 X. Wang, X. Han, R. Du, C. Xing, X. Qi, Z. Liang, P. Guardia, J. Arbiol, A. Cabot and J. Li, *ACS Applied Materials & Interfaces*, 2022, **14**, 41924–41933.

48 L. Wu, L. Yu, B. McElhenny, X. Xing, D. Luo, F. Zhang, J. Bao, S. Chen and Z. Ren, *Applied Catalysis B: Environmental*, 2021, **294**, 120256.

49 H. Chen, S. Zhang, Q. Liu, P. Yu, J. Luo, G. Hu and X. Liu, *Inorganic Chemistry Communications*, 2022, **146**, 110170.

50 C. Ros, S. Murcia-López, X. Garcia, M. Rosado, J. Arbiol, J. Llorca and J. R. Morante, *ChemSusChem*, 2021, **14**, 2872–2881.

51 Y. Yao, S. Sun, H. Zhang, Z. Li, C. Yang, Z. Cai, X. He, K. Dong, Y. Luo, Y. Wang, Y. Ren, Q. Liu, D. Zheng, W. Zhuang, B. Tang, X. Sun and W. (Walter) Hu, *Journal of Energy Chemistry*, 2024, **91**, 306–312.

52 J. George, G. Petretto, A. Naik, M. Esters, A. J. Jackson, R. Nelson, R. Dronskowski, G. Rignanese and G. Hautier, *ChemPlusChem*, DOI:10.1002/cplu.202200123.

53 C. Xiong, S. Dai, Z. Wu and D. Jiang, *ChemCatChem*, DOI:10.1002/cctc.202200133.

54 G. Henkelman, B. P. Uberuaga and H. Jónsson, *The Journal of Chemical Physics*, 2000, **113**, 9901–9904.

55 G. Henkelman and H. Jónsson, *The Journal of Chemical Physics*, 2000, **113**, 9978–9985.